

1 **Synchronous activity patterns in the dentate gyrus during immobility**

2

3 Martin Pofahl¹, Negar Nikbakht¹, André N. Haubrich¹, Theresa Nguyen¹, Nicola Masala¹,
4 Fabian Distler¹, Oliver Braganza¹, Jakob H. Macke², Laura A. Ewell¹, Kurtulus Golcuk¹ and
5 Heinz Beck^{1,3*}

6 ¹ Institute for Experimental Epileptology and Cognition Research, University of Bonn,
7 Germany

8 ² Machine Learning in Science, Cluster of Excellence "Machine Learning", University of
9 Tübingen, Germany & Department Empirical Inference, Max Planck Institute for Intelligent
10 Systems, Tübingen, Germany

11 ³ Deutsches Zentrum für Neurodegenerative Erkrankungen e.V., Bonn, Germany

12

13 * Correspondence should be addressed to:

14 Heinz Beck
15 Institute for Experimental Epileptology and Cognition Research Epileptology
16 University of Bonn
17 Sigmund-Freud Str. 25
18 53105 Bonn
19 Tel.: 0228 6885 270
20 Fax: 0228 6885 294
21 e-mail: Heinz.beck@ukbonn.de

22

23

24

25 Figures: 8

26 Figure Supplements: 11

27 Supplementary Videos: 2

28 Supplementary Files: 1

29

30 **Abstract**

31 The hippocampal dentate gyrus is an important relay conveying sensory information from the
32 entorhinal cortex to the hippocampus proper. During exploration, the dentate gyrus has been
33 proposed to act as a pattern separator. However, the dentate gyrus also shows structured
34 activity during immobility and sleep. The properties of these activity patterns at cellular
35 resolution, and their role in hippocampal-dependent memory processes have remained
36 unclear. Using dual-color in-vivo two-photon Ca^{2+} imaging, we show that in immobile mice
37 dentate granule cells generate sparse, synchronized activity patterns associated with
38 entorhinal cortex activation. These population events are structured and modified by changes
39 in the environment; and they incorporate place- and speed cells. Importantly, they are more
40 similar than expected by chance to population patterns evoked during self-motion. Using
41 optogenetic inhibition, we show that granule cell activity is not only required during
42 exploration, but also during immobility in order to form dentate gyrus-dependent spatial
43 memories.

44

45 **Keywords:** Hippocampus, dentate gyrus, spatial learning, pattern separation, memory

46

47

48

49 **Introduction**

50 The dentate gyrus receives polymodal sensory information from the entorhinal cortex, and
51 relays it into the hippocampal network. The most prevalent view of the dentate gyrus input-
52 output transformation in this circuit is that it acts as a pattern separator. This capability
53 requires the animal to generate dissimilar neuronal representations from overlapping input
54 states that represent similar but not identical environments (**Cayco-Gajic and Silver, 2019**).
55 Such an operation, termed pattern separation, has been ascribed to the hippocampal dentate
56 gyrus in species ranging from rodents to humans (**Berron et al., 2016; Leutgeb et al.,**
57 **2007; Sakon and Suzuki, 2019**). In the dentate gyrus, polysensory inputs are mapped onto
58 a large number of granule cells which exhibit extremely sparse firing patterns, resulting in a
59 high probability of non-overlapping output patterns (**Danielson et al., 2016; GoodSmith et**
60 **al., 2017; Hainmueller and Bartos, 2018; Pilz et al., 2016; Senzai and Buzsáki, 2017; van**
61 **Dijk and Fenton, 2018**). This concept has been influential in understanding dentate gyrus
62 function when processing multimodal, current or 'online' sensory information during mobility
63 and exploration.

64 However, the dentate gyrus is far from silent during immobility. It displays prominent
65 electrographic activity patterns such as dentate spikes and sharp waves, which occur
66 primarily during immobility or sleep (**Bragin et al., 1995; Meier et al., 2020; Penttonen et**
67 **al., 1997**). In downstream hippocampal regions such as CA1, neuronal activity during
68 immobility incorporates the replay of behaviorally relevant sequences during sharp wave
69 ripples, a process important in memory consolidation (**Davidson et al., 2009; Diba and**
70 **Buzsáki, 2007; Dupret et al., 2010; Foster and Wilson, 2006; Girardeau et al., 2009;**
71 **Malvache et al., 2016; Skaggs and McNaughton, 1996; Wilson and McNaughton, 1994**).
72 In the dentate gyrus, little detail is known about how granule cells are active during immobility
73 at the population level, and it is unknown whether activity during immobility reiterates
74 behaviorally relevant information. Moreover, the role of dentate gyrus activity during
75 immobility in memory formation is unclear.

76 Here, we have used dual-color two-photon in-vivo Ca^{2+} imaging to show that in immobile
77 mice, the dentate gyrus exhibits frequent, sparse and synchronous population events that at
78 the population level are similar to activity patterns during locomotion. Moreover, we have
79 tested the idea that dentate gyrus activity during immobility is relevant for dentate-gyrus
80 dependent spatial memory.

81

82

83 Results

84 ***Sparse, structured dentate network events in immobile animals***

85 We imaged the activity of large populations of hippocampal dentate granule cells (GCs)
86 using a Thy1-GCaMP6s mouse line (GP4.12Dkim/J, (*Dana et al., 2014*)). In addition, we
87 monitored the bulk activity of the major input system into the dentate gyrus, the medial
88 perforant path (MPP). To this end, we expressed the red-shifted Ca²⁺ indicator jRGECO1a
89 (*Dana et al., 2016*) in the medial entorhinal cortex using viral gene transfer (see Methods
90 section, **Fig. 1A, Fig. 1-figure supplement 1A**). To allow efficient excitation of both
91 genetically encoded Ca²⁺ indicators, we established excitation with two pulsed laser sources
92 at 940 and 1070 nm (see **Fig. 1-figure supplement 1B-F**). The mice were placed under a
93 two-photon microscope and ran on different variants of a linear track, equipped with different
94 types of cues (see **Fig. 1-figure supplement 1G-J, Video 1**).

95 As previously described, the firing of GCs was generally sparse (*Danielson et al., 2016*;
96 *Hainmueller and Bartos, 2018*; *Neunuebel and Knierim, 2012*; *Pilz et al., 2016*), both
97 when animals were immobile and when they were running on a textured belt without
98 additional cues (mean event frequency 1.38±0.19 events/min and 0.97±0.2 events/min,
99 respectively, n=1415 granule cells in 9 mice, **Fig. 1B, Fig. 1-figure supplement 2C-E**).
100 Despite the sparse activity of granule cells, we observed synchronized activity patterns
101 (**Video 2**). To rigorously define such events, we used an algorithm that detects synchronized
102 network events within a 200 ms time window, corresponding to 1±1 frame at our sampling
103 rate (see Methods). Such synchronous network events could readily be observed in the
104 dentate gyrus in all mice (**Fig. 1C, D**, network events depicted in different colors, see
105 examples for $\Delta F/F$ traces of participating cells in **Fig. 1E**). Network events were sparse,
106 incorporating on average only 5.7±0.09 % of the total active GC population. Shuffling
107 analysis (see Methods) confirmed that network events do not arise by chance (**Fig 1F**, grey
108 bars correspond to shuffled data, n=9 mice, 3 sessions/mouse). This was robust over three
109 different types of shuffling analysis (**Fig. 1G, Fig. 1-figure supplement 3** and Methods for
110 the description of the shuffling methods).

111 Notably, network events occurred mainly during immobility periods and were much less
112 prevalent during running (**Fig. 1D**, quantification in **Fig. 1G**). Accordingly, network event
113 frequencies were significantly higher during immobility (repeated measures ANOVA,
114 $F_{(1,8)}=117$, $p=2 \times 10^{-6}$, $n=9$ mice, 3 sessions, **Fig. 1H**). During immobility periods (defined as
115 running speeds <4 cm/s), the vast majority of (99.6%) network events occurred when mice
116 were completely immobile. Network events were on average evenly distributed during the
117 20-minute imaging session (**Fig. 1I**), as well as during individual periods of immobility (**Fig.**
118 **1J**).

119

120 ***Dentate network events are correlated with MPP activation***

121 We then analyzed the activity in the MPP input fiber tract expressing jRGECO, and probed
122 the relation of this activity with GC activity patterns. As expected during exploratory states,
123 the bulk MPP activity was increased during locomotion, consistent with increased sensory
124 input (**Fig. 2A, B**, red channel, **Fig. 2C** for average value). During immobility in particular,
125 larger fluctuations of bulk MPP activity were observed. This phenomenon was reflected in a
126 larger variance of the bulk MPP signal during immobility (**Fig. 2D**). Cross-correlation revealed
127 that during immobility, the increases in bulk MPP activity were associated with peaks in
128 average GC activity levels (**Fig. 2E**). Both signals were significantly correlated in most
129 sessions for periods of immobility, (8/9 sessions, $n=3$ mice, 3 sessions per mouse, Granger
130 causality test $p < 0.05$). This correlation was clearly visible during network events, because
131 aligning GC activity and MPP activity to the timepoint of network events revealed a strong
132 coactivation of GC and MPP during network events (**Fig. 2F**, $n=3$ mice). During running,
133 MPP signals did not correlate with average GC activity, which is not unexpected given the
134 asynchronous activation of GCs during running. (8/9 sessions, Granger causality test
135 $p > 0.05$).

136 To explore in more detail how individual fluctuations in MPP bulk activity are associated with
137 GC activity, we used a deconvolution algorithm to identify synchronous activity of MPP axons

138 visible in the bulk MPP transients (see Methods). We then quantified amplitude and
139 frequency of these transients during locomotion and immobility. First, we found that bulk
140 MPP events detected during immobility are on average larger than those detected during
141 running (**Fig. 2G**, Kruskal-Wallis test, $n=3$ mice, 3 sessions per mouse, 8469 and 19106
142 events during running and resting, respectively, $p=2 \times 10^{-44}$), in agreement with the larger
143 variance of the MPP signal during these periods. When we examined the frequencies of all
144 detected MPP bulk events during locomotion and immobility, we found that there were
145 significantly more events during running (repeated measures ANOVA, $F_{(1,2)}=255$, $p=3 \times 10^{-6}$,
146 $n=3$ mice, 3 sessions, **Fig. 2H**). However, large events, defined as bulk MPP events with
147 amplitudes above two standard deviations of the mean, were significantly more frequent
148 during resting states (repeated measures ANOVA, $F_{(1,2)}=27$, $p=2 \times 10^{-3}$, $n=3$ mice, 3 sessions,
149 **Fig. 2I**). Again, this is consistent with the larger variance of the MPP signal during immobility,
150 and likely reflects synchronized activation of MPP fibers. In line with the correlation of MPP
151 and GC signals, there was a short temporal delay between individual bulk MPP transients
152 and network events (**Fig. 2J**).

153

154 ***Dentate network events are correlated with pupil constriction***

155 Pupil diameter is an indicator of neuronal state and arousal (**Reimer et al., 2014; Reimer et**
156 **al., 2016**), and can be used to track changes in neuronal states during quiet wakefulness
157 (**Reimer et al., 2014**). Of note, pupil changes have been shown to closely track the rate of
158 occurrence of hippocampal synchronous activity, namely sharp waves in the hippocampal
159 CA1 region (**McGinley et al., 2015**). We therefore asked if dentate network events are also
160 associated with specific changes in pupil diameter (**Fig. 3A** for example measurement of
161 pupil diameter over multiple resting and locomotor states). As previously described (**Reimer**
162 **et al., 2014; Reimer et al., 2016**), we found pupil constriction during immobility with dilation
163 at locomotion onsets (**Fig. 3B, C**, $n=6$ mice, 3 sessions). Intriguingly, the average pupil
164 diameters during network events were significantly more constricted compared to the

165 average pupil diameters during entire periods of immobility (**Fig. 3D**, repeated measures
166 ANOVA for all three groups $F_{(2,28)}=17.17$, $p=1 \times 10^{-5}$, $n=6$, data from 3 sessions each,
167 Bonferroni post-tests: pupil diameters during locomotion vs. immobility $p=0.0068$, locomotion
168 vs. network events $p=0.0016$, immobility vs. network events $p=0.0017$).

169 When looking at pupillary dynamics by assessing the rate of diameter change, locomotor
170 episodes were on average associated with pupil dilation, while network events were
171 specifically associated with pupil constriction (**Fig. 3E**, repeated measures ANOVA
172 $F_{(2,28)}=34.18$, $p=3 \times 10^{-8}$, $n=6$ mice, data from 3 sessions each, Bonferroni post-tests: pupil
173 diameters during locomotion vs. immobility $p=0.0016$, locomotion vs. network events
174 $p=2.53 \times 10^{-5}$, immobility vs. network events $p=0.00053$). The latter finding was clearly
175 illustrated by averaging pupil diameters aligned to NE times (**Fig. 3F**). Together, this
176 suggests that network events are associated with specific pupillary dynamics reflecting
177 substates of arousal and neuronal synchronization during immobility.

178

179 ***Network events are more orthogonal than expected by chance, but repetitively recruit***
180 ***GC sub-ensembles***

181 We then further characterized the participation of dentate granule cells in network events.
182 We first asked to what extent individual network events recruit orthogonal cell populations.
183 Indeed, while individual GCs can partake in multiple network events (see **Fig. 1C, D, Video**
184 **2**), we also observed network events that seemed completely distinct to others. To quantify
185 how similar network events are to one another, we computed population vectors for each
186 network event. We then computed the cosine similarity as a measure of similarity between
187 vectors representing individual network events (see Methods). With this measure, network
188 event pairs recruiting the same set of neurons have a cosine similarity of 1, and completely
189 orthogonal patterns exhibit a cosine similarity of 0. This analysis revealed that 38% of
190 network event pairs were completely orthogonal to one another (**Fig. 4A**, the fraction of
191 completely orthogonal patterns corresponds to the bar with a cosine similarity of zero).

192 Because in sparse activity patterns, orthogonality can and will arise by chance, we
193 additionally performed a shuffling analysis to ascertain if sparse activity per se can account
194 for the observed occurrence of orthogonal patterns. We found significantly more
195 orthogonality than expected by chance ($38\pm 4\%$ vs. $29\pm 4\%$ in real vs. shuffled data,
196 respectively, see **Fig. 4A** inset, $n=9$ mice, 3 sessions, comparison to shuffled data: Wilcoxon
197 test, $p=0.0039$). This is consistent with the capability to represent separate sets of
198 information within network events.

199 Even though orthogonal network events were observed, we also observed a repeated
200 activation of granule cells in multiple network events (see i.e. **Video 2**). To examine if specific
201 sub-ensembles of granule cells are repeatedly recruited in network events, we performed a
202 pairwise Pearson's correlation of the activity of all cell pairs during all network events of a
203 recording session (correlation coefficients depicted in the correlation matrix in **Fig. 4B**). We
204 then re-arranged the cells by hierarchical clustering. Clusters were combined using a
205 standardized Euclidean distance metric and a weighted average linkage method (**Fig. 4C**,
206 more examples in **Fig. 4-figure supplement 1A-H**).

207 This visualization reveals the existence of subgroups of cells that are strongly correlated
208 within network event-related activity (**Fig. 4C**), as previously demonstrated for activity during
209 immobility in the CA1 region (*Malvache et al., 2016*). To more rigorously define what we
210 considered a cluster showing correlated activity, we used a comparison to a null distribution
211 generated by shuffling. Such approaches have been shown to outperform other approaches
212 to define how many clusters are present in complex data (*Tibshirani et al., 2001*). We
213 combined clusters until the mean of the cluster internal r -value reached a significance
214 threshold, which was defined by creating a null-distribution of r -values from shuffled datasets
215 (indicated with a vertical line in **Fig. 4C**). Thus, clusters were defined quantitatively as
216 exhibiting a mean correlation coefficient within the cluster above chance level. Using this
217 definition, the average cluster size was 6.7 ± 0.4 cells per cluster ($n=9$ mice, 3 sessions). The
218 repetitive nature of GC cluster activation during an entire session becomes clearly apparent

219 when viewing cell activity during network events over an entire session, sorted by their
220 participation in clusters (example shown in **Fig. 4D**).

221

222 ***Participation of place- and speed-coding granule cells in network events***

223 To ask if network events carry specific spatial or locomotion-related information, we identified
224 GCs with position-related or speed-related activity. We first identified the group of GCs that
225 exhibited significant place coding (2.83% of n=1415 active cells imaged in 9 mice, **Fig. 5A** for
226 representative polar plots of three GCs). The place fields of place-coding GCs were
227 distributed over the linear track (**Fig. 5B**). If the fraction of place-coding cells was calculated
228 as a fraction of only those GCs active during running, the fraction of significantly place-
229 coding GCs was 6.09%. Secondly, we identified a fraction of GCs (0.85% of GCs, 1.83% of
230 running-active GCs, n=9 mice) displaying a significant correlation of activity with running
231 speed (**Fig. 5C-E**). This is in contrast to a previous study (*Danielson et al., 2016*), but
232 consistent with data obtained in freely moving mice (*Stefanini et al., 2020*). We also
233 examined recordings from sessions using two other linear track environments with sensory
234 cues placed on the textured belt. First, additional sensory cues were placed randomly on the
235 belt (cue-enriched condition). Under these conditions, the fraction of place cells observed
236 within the GC population increased (4.56% of GCs, 10.74% of running-active GCs), as did
237 the proportion of speed cells (1.54% of GCs, 3.64% of running-active GCs, n=1425 active
238 GCs imaged in 9 mice, **Fig. 5F**).

239 Second, we tested if there is a further increase in place cells with a commonly used linear
240 track divided into zones, each with very different spatial cues (see methods, **Fig. 1-figure**
241 **supplement 1G-J**). This was not the case. In these mice (n=3), we recorded 690 GCs, of
242 which 2.61% were place cells. As a fraction of those GCs active during running, we found
243 8.11% place cells. In all conditions, few cells exhibited both speed coding and place coding.

244 We then examined if place or speed cells are incorporated in network events, and if this
245 participation is altered when the environment changes. Specifically, we examined the

246 difference between the baseline linear track without additional cues and the cue-enriched
247 condition. We chose the cue-enriched condition for further experiments and analyses
248 because it provided sufficient spatial cues for a strong spatial representation, without
249 introducing edges between differently cued zones on the linear track. We found that in the
250 cue-enriched condition, dentate gyrus network events were again observed predominantly
251 during immobility (**Fig. 5-figure supplement 1D**, statistics of GC activity in **Fig. 5-figure**
252 **supplement 1A-C**) and were similarly related to MPP activity (**Fig. 5-figure supplement 1F-**
253 **J**). Increasing the cue density did not significantly alter the network event frequency (**Fig. 5-**
254 **figure supplement 1D**, 2.39 ± 0.73 vs 3.63 ± 0.90 events/minute, respectively, $n=9$ mice, 2-
255 way ANOVA, baseline vs. cue enriched: $F_{(1,30)}=0.71$, $p=0.41$, run vs. rest: $F_{(1,3)}=59.13$,
256 $p=0.001$). However, the average size of individual network events, measured as the number
257 of participating GCs, was significantly larger in the cue-enriched condition compared to the
258 baseline condition (**Fig. 6A**, Kruskal-Wallis test, $n=9$ mice, 1313 and 1493 network events in
259 baseline and cue-enriched condition, respectively, $p=4 \times 10^{-41}$), with individual GCs
260 contributing more frequently to network events in the cue-rich condition (**Fig. 6B**, Kruskal-
261 Wallis test, $p=1 \times 10^{-40}$). Fewer orthogonal networks were observed in the cue-rich condition,
262 but this was not significantly different to the baseline condition (not shown, Kruskal-Wallis
263 test, n.s. $p=0.49$).

264 We then examined if the participation of place and speed cells in network events is altered in
265 the cue-enriched compared to the baseline condition. As stated above, place cells are more
266 commonly observed in cue-enriched sessions. However, when we calculated the fraction of
267 all place cells that participated in network events, taking into account the total number of
268 place cells under each condition, the probability of being incorporated in network events was
269 increased significantly (**Fig. 6C**, 55.42 vs. 88.46% of place cells in baseline vs. cue-rich
270 conditions). This was not the case for speed cells (42.86 vs. 52.63% of speed cells in
271 baseline vs. cue-rich conditions, $n=9$ mice, χ^2 test regarding changes in the incorporation of
272 place and speed cells in network events $p=3 \times 10^{-4}$, post-test: place cells baseline vs. cue-
273 enriched $p=1 \times 10^{-5}$, indicated with asterisk in **Fig. 6C**, speed cells baseline vs. cue-enriched

274 p=0.22). Thus, irrespective of the increase in the number of place cells in cue-enriched
275 conditions, the probability of individual place cell to be integrated a network event is
276 significantly higher. Accordingly, the proportion of synchronous events that incorporated at
277 least one place cell increased (from 23±9 to 33±11%). The properties of correlated cell
278 clusters within network events did not change (cluster size comparison, Kruskal-Wallis test, n
279 = 9 mice, p = 0.13), but significantly more of the clusters contained place cells in the cue-rich
280 condition (**Fig. 6D**, n = 9 mice, Chi² test p = 0.004, post-test comparison baseline vs. cue-
281 enriched for place cells p = 0.004, speed cells p = 0.6), with the number of place or speed
282 cells per cluster remaining unchanged (**Fig. 6E**).

283 Thus, network events are responsive to changes in the environment, and incorporate more
284 place-coding neurons into correlated activity patterns.

285

286 ***Similarity of population activity patterns during locomotion to network events during*** 287 ***immobility***

288 The incorporation of place and speed cells in network events, as well as the fact that
289 changing features of the environment modifies network event size and place cell participation
290 is consistent with the idea that animals, when immobile, represent information about the
291 environment in synchronous, sparse network events. Testing this idea is difficult, however,
292 given that place cells are less prevalent in the dentate gyrus compared to other hippocampal
293 sub-regions. It has been suggested that the dentate gyrus utilizes a population code
294 (**Stefanini et al., 2020**), meaning that even though only few cells can be rigorously classified
295 as place cells, many more neurons may encode relevant but partial information about the
296 environment. We used three different approaches to assess similarity between running and
297 resting activity in the dentate gyrus at the population level. All of these approaches are based
298 on analyzing population coding separately during either locomotion or network events using
299 Principal Component Analysis (PCA).

300 To obtain a first visual impression of population behavior during linear track locomotion, we
301 plotted the neuronal state captured by the first three components (**Fig. 7B, C, Fig. 7-figure**
302 **supplement 1B-C** for Independent Component Analysis, ICA, and Gaussian Process Factor
303 Analysis, GPFA). We observed smooth, large trajectories with high variability reflecting
304 movement along the linear track for some laps on the linear treadmill. Such large trajectories
305 did not occur for every lap. We examined this unexpected phenomenon in both the baseline
306 and cue-enriched condition (**Fig. 7-figure supplement 2A, B**), as well as in the belt with
307 three distinct zones (**Fig. 7-figure supplement 2C**). In all three types of linear tracks, we
308 found a similar, high lap to lap variability in the dentate gyrus population. To see how this
309 behavior compares to the CA1 region, which is known to exhibit a reliable place code over
310 these timeframes (*Rubin et al., 2019*), we examined CA1 neurons in mice running on a
311 linear track with zones (n=2 mice, 543 CA1 neurons, identical conditions to the zoned belt
312 used for GC measurements). Here, PCA trajectories showed a much lower lap-to-lap
313 variability and related smoothly to the position on the linear track (**Fig. 7C, Fig. 7-figure**
314 **supplement 1D-F**, for PCA, GPFA, ICA, see Methods, and **Fig. 7-figure supplement 2D**).
315 We have quantified this phenomenon across all laps in a session by plotting the weights of
316 the first 5 components of the PCA across laps. In this depiction for CA1, as well as the three
317 different versions of the linear track used for DG experiments, it is very clear that strong
318 periodicity for each round is observed in CA1, but much less so in all DG experiments (**Fig.**
319 **7-figure supplement 2E-H**).

320 To quantify the strength of lap-periodicity (i.e. population spatial stability throughout a
321 session) across animals, we performed an autocorrelation for all experiments in the four
322 conditions. The autocorrelation showed large magnitude peaks at integer multiples of 1 lap
323 for CA1, which were significantly larger than corresponding peaks for all linear track
324 conditions in DG (examples shown in **Fig. 7-figure supplement 2I-L**, averages across all
325 mice and sessions **Fig. 7-figure supplement 2M-P**, statistics **Fig. 7D** ANOVA, $F_{(1,3)}=88.32$,
326 $p=2 \times 10^{-30}$, * Bonferroni post-test $p < 0.05$, *** Bonferroni post-test $p < 0.001$).

327 Thus, the population behavior in DG was similar across three different types of linear track,
328 with an episodic nature that was clearly distinct from the repetitive, stable population
329 dynamics in CA1.

330 After applying PCA to locomotor states in the dentate gyrus, we then also performed a PCA
331 analysis of population activity during network events, including the number of components
332 explaining 50% of the variance (see Methods, **Fig. 7E** for schematic description). In order to
333 compare the two sets of PCAs representing population activity during running states and
334 network events, respectively, we first used a vector-based similarity measure. Briefly, we
335 projected the traces recorded during locomotion into the PCA-space representing activity
336 during network events, and tested how much of their variance was captured by them. In this
337 analysis, similarity between both population measures would result in a large fraction of
338 explained variance (**Fig. 7F**).

339 To obtain the expected null distribution, we performed different types of shuffling analysis on
340 the resting activity (see Methods). In the first shuffling procedure, we shifted the entire $\Delta F/F$
341 time series of each cell by random time values (compare **Fig. 7H, I**). Thus, all non-random
342 activity timing between cells is destroyed and cells will no longer be synchronously active at
343 NE timepoints. At the same time, individual cell event statistics will be maintained (i.e. inter-
344 event-intervals). This method thus preserves intra-neuronal correlations and event
345 frequencies, but destroys inter-neuronal correlations. The distributions from shuffled data
346 were clearly distinct from the real data (red vertical line in **Fig. 7G, Fig. 7-figure supplement**
347 **3** for comparisons to shuffled data for all sessions). The comparisons to shuffled data were
348 significant in all sessions, both for baseline and cue-enriched conditions (**Fig. 7I**, leftmost
349 bars in lower panel), indicating that synchronous activity is important for the similarity
350 between locomotor related activity and network events.

351 We used two further similarity measures that have been used so far to quantify similarity
352 between PCA bases. Firstly, we used a similarity factor S_{PCA} as described by Krzanowski
353 (**Krzanowski, 1979**) and the EROS similarity factor (**Yang, K., Shahabi, C., 2004**) (see

354 Methods for description), testing them against shuffled datasets in the same manner (**Fig. 7I**,
355 **Fig. 7-figure supplement 3** for comparisons to shuffled data for all sessions). With these
356 measures, significant comparisons to shuffled data were obtained with all (cosine similarity)
357 or a majority (EROS) of sessions (**Fig. 7I**, n=8 animals, last baseline session and cue-
358 enriched session).

359 This shuffling approach (**Fig. 7I**), however, does not specifically test if the composition of
360 NEs matters for the similarity between running and NE activity. We therefore implemented
361 two additional shuffling approaches that probe the importance of NE structure by shuffling
362 activity within NEs. In our second shuffling approach, we tested if the composition of
363 individual NEs is important. To this end, for each individual NE, we randomly reassigned a
364 given cells activity to a different cell. Thus, NEs have exactly the same number of active
365 cell's, but the identity of cells active within them has been randomly changed, and the
366 number of NEs that individual cells participate in will be altered (see schematic in **Fig. 7J**,
367 compare to panel H). This shuffling approach also revealed that NEs are significantly more
368 similar to locomotor related activity with all three similarity measures (**Fig. 7J**, lower panel).

369 If morpho-functional properties in the network simply confine activity during run and rest to
370 very specific populations of cells that are always very active, then a different type of shuffling
371 would be required to test if this phenomenon drives similarity. We therefore added a third
372 shuffling method, in which for each cell, we randomly reassigned its NE activity to other NEs
373 (see schematic in **Fig. 7K**, cf. panel H). Thus, how many NEs a given cell participates in is
374 maintained. At the same time, NE interactions between specific sets of cells will be altered,
375 although highly active cells that participate in multiple NEs will still be more likely to be co-
376 active in shuffled NEs. If the similarity were driven by such a population of always-active
377 cells, then this shuffling would not disrupt the similarity between running and shuffled NE
378 activity. However, also here NE activity was more similar to running activity than shuffled
379 data for all three similarity measures (**Fig. 7K**, lower panel).

380 Collectively, these data show that at the population level, NEs and locomotion related activity
381 are more similar than expected by chance. Moreover, the two shuffling procedures described
382 in Fig. 7J and K suggest that the cellular composition of network events matters for this
383 similarity.

384 In CA1, replay of place cell sequences has been described extensively. To ascertain the
385 robustness of our similarity measures, we have applied them to CA1 population activity, in
386 exactly the same manner as described in **Fig. 7F**. This approach showed significant
387 similarities between synchronous CA1 events during immobility, and activity during
388 locomotion in 100 % of the tested sessions for all three PCA-based measures (5 mice, 3
389 sessions per mouse, data not shown).

390

391 ***Inhibition of dentate granule cell activity during immobility disrupts pattern separation***

392 Collectively, these data suggest that during immobility, GCs engage in structured ensemble
393 activity that reiterates activity during running at the population level. This suggests that such
394 activity might be important for the formation of hippocampal dependent spatial memories.
395 The ideal test of this hypothesis would be to detect network events in freely moving animals
396 using two-photon imaging during a memory task, and then applying closed-loop inhibition of
397 granule cells during this task. The sparseness of granule cell activity, and the difficulties
398 inherent in triggering closed-loop inhibition to very sparse activity patterns renders this
399 experiment extraordinarily difficult. We therefore opted to use closed-loop inhibition of
400 granule cells during all periods of immobility during a dentate gyrus-dependent memory task
401 to test if dentate gyrus activity during immobility is necessary for memory formation. We used
402 an established memory task for spatial object pattern separation (OPS, (**van Goethem et al.,**
403 **2018**)), in which DG-dependent spatial discrimination is assessed based on the differential
404 exploration of two objects. Briefly, animals are first exposed to two objects in defined
405 locations during an acquisition trial (5 min) and are then re-exposed following an intermediate

406 period, with one of the objects slightly displaced. Increased exploration of the displaced
407 object indicates that the animal has encoded the initial location and is able to discriminate the
408 displaced object. In preliminary experiments, we tested 4 degrees of object displacement
409 along a vertical axis (3-12 cm, **Fig. 8-figure supplement 1C**). We then determined the
410 extent to which spatial object pattern separation was dependent on the activity of the dentate
411 gyrus. We expressed either halorhodopsin (eNpHR, (*Gradinaru et al., 2008*)), or eYFP
412 (control group) selectively in dentate GCs using Prox1-Cre mice, which efficiently inhibited
413 GC firing (**Fig. 8-figure supplement 1F-J**), and bilaterally illuminated the dentate gyrus with
414 two implanted light fibers during the OPS task (**Fig. 8-figure supplement 1A, B, D**). We
415 found that GC activity was most important for an intermediate degree of displacement (9 cm),
416 while maximal displacement was no longer dependent on GC activity (**Fig. 8-figure
417 supplement 1E**).

418 We then used this intermediate degree of displacement for the further experiments. We first
419 inhibited GCs during locomotion only in the learning trial. As expected, inhibiting GC activity
420 when mice actively explored the environment to be memorized led to a loss of preference for
421 the displaced object in the subsequent recall trials (**Fig. 8-figure supplement 2**).

422 We then used the intermediate degree of displacement in the OPS task to see if dentate
423 gyrus activity during quiet immobility was equally required to establish a memory of object
424 location. We bilaterally inhibited GCs during periods of quiet immobility (running speed < 4
425 cm/s) only during the learning trial (**Fig. 8A, B**). This manipulation led to a complete loss of
426 preference for the displaced object in the subsequent recall trials (**Fig. 8H** for representative
427 sessions, analysis of discrimination index in **I**, unpaired T-test with Welch's correction, n = 6
428 and 9 for eNpHR and eYFP respectively, $t_{(12)} = 5.37$, $p = 0.0002$) whereas control mice
429 displayed a clear preference for the displaced object (**Fig. 8G** for representative session).
430 Similar results were obtained in a separate cohort of animals, where the difference in
431 performance was measured in a paired experimental design (**Fig. 8-figure supplement 2**,
432 repeated measures ANOVA, $F_{(1,14)} = 54.58$, $p = 0.0003$. Bonferroni post-tests: no illumination

433 vs. resting illumination, $p = 0.0026$; no illumination vs. illumination during locomotion, $p =$
434 0.0076 ; $n = 5$).

435 Carrying out the OPS task in mice expressing eNpHR without illumination yielded
436 discrimination indices indistinguishable from the control group (not shown). For the three
437 groups, ANOVA revealed a significant effect ($F_{(2,18)} = 8.52$, $p = 0.003$), with Bonferroni post-
438 tests showing that inhibition of GCs significantly reduces performance vs. the two control
439 groups (eYFP vs. eNpHR illuminated $p = 0.006$, eYFP vs. eNpHR without illumination $p >$
440 0.99 , eNpHR with illumination vs. without illumination $p = 0.006$).

441 Because mice are also immobile while examining the objects, we also performed a set of
442 experiments in which light-stimulation was only carried out during immobility, but excluding a
443 4 cm zone surrounding the objects (**Fig. 8-figure supplement 3A**). This experiment yielded
444 similar results, with a virtually complete loss of object discrimination during the recall trial
445 (**Fig. 8-figure supplement 3B-I**). This effect was specific to acquisition. GC inhibition only
446 during immobility in the recall trial (**Fig. 8-figure supplement 3J**) elicited no significant
447 reduction in the recognition of the displaced object (**Fig. 8-figure supplement 3K-L**, $n = 11$
448 and 6 for eYFP and eNpHR groups, respectively, t-test with Welch correction n.s.). These
449 data suggest that activity of GCs during rest is important to form memories that require
450 discrimination of similar experiences.

451

452 **Discussion**

453 The dentate gyrus has been implicated in pattern separation of sensory-driven activity
454 patterns during experience but is also active during immobility and sleep. The properties of
455 these latter forms of activity at the cellular level and the role they play in behavior are largely
456 unknown. The application of multiphoton in-vivo Ca^{2+} imaging allowed us to observe large-
457 scale dentate gyrus dynamics at the cellular level and to detect a novel form of sparse,
458 synchronized GC activity that occurs during immobility, termed dentate network events.
459 These events were specifically modified by the environment, and showed higher similarity
460 than expected by chance to population activity occurring during locomotion, indicating a
461 sparse reiteration of locomotion-associated activity patterns.

462 Interestingly, network events were associated with pupil constriction and on average smaller
463 pupil diameters when compared to entire periods of immobility, indicating that they may be
464 associated with fluctuations in brain state during immobility, as described for visual cortex
465 (*Reimer et al., 2014*). This finding is in agreement with the correlation of pupil constriction
466 with the rate of hippocampal ripple oscillations during resting states (*McGinley et al., 2015*).
467 The association of pupil constriction with synchronized activity is also very consistent with
468 data from visual cortex, where brief episodes of pupil constriction during immobility are
469 associated with synchronization and increased low-frequency oscillations (*Reimer et al.,*
470 *2014*).

471 For neuronal activity during resting states to support learning or memory consolidation
472 concerning a particular environment, one general requirement would be that there is
473 reactivation of activity patterns induced by exploration of the relevant environment
474 (*Davidson et al., 2009; Diba and Buzsáki, 2007; Dupret et al., 2010; Foster and Wilson,*
475 *2006; Girardeau et al., 2009; Skaggs and McNaughton, 1996; Wilson and McNaughton,*
476 *1994*). We have used three different similarity measures to show that this is the case in the
477 dentate gyrus at the population level.

478 In addition to this general requirement, two specific features of resting activity are consistent
479 with the formation of precise memories that conserve the pattern separation capabilities of
480 the dentate gyrus. Firstly, the activity patterns, although sparse, should be capable of
481 generating orthogonal ensembles representing different features of the environment.
482 Secondly, the activity should repetitively recruit specific subsets of dentate GCs capable of
483 instructing the formation of CA3 attractors via Hebbian plasticity mechanisms. Indeed, we
484 found that activity during network events is sparse, recruiting just ~5-7% of the active GCs.
485 Given that only ~50% of GCs are active in head-fixed animals (*Danielson et al., 2016; Pilz*
486 *et al., 2016*), recruitment of dentate GCs during network events is much sparser than in other
487 forms of activity occurring during immobility or sleep. For instance, the fraction of CA1
488 neurons recruited during sharp wave ripple mediated replay of behaviorally relevant
489 sequences (*Davidson et al., 2009; Diba and Buzsáki, 2007; Dupret et al., 2010; Foster*
490 *and Wilson, 2006; Girardeau et al., 2009; Malvache et al., 2016; Skaggs and*
491 *McNaughton, 1996; Wilson and McNaughton, 1994*) is much higher than the recruitment
492 of GCs in network events. One consequence of the sparseness of network events is that
493 they are predicted to recruit highly constrained CA3 ensembles, both because of the sparse
494 excitatory connectivity of mossy fibers in CA3, and because of the properties of the powerful
495 inhibitory circuits in the CA3 region (*Acsady et al., 1998; Neubrandt et al., 2017;*
496 *Neubrandt et al., 2018*). This has been suggested to be important in the capability to store
497 information in CA3, while conserving the pattern separation benefits of the dentate gyrus
498 (*O'Reilly and McClelland, 1994; GoodSmith et al., 2019*).

499 We found that network events are structured, with subgroups of dentate GCs forming
500 correlated sub-ensembles that are repeatedly recruited (see **Fig. 4**). This finding is consistent
501 with the idea that dentate GC activity recruits plasticity mechanisms to form sparse attractor-
502 like representations in CA3 (*O'Reilly and McClelland, 1994*). A similar structure was also
503 observed for awake hippocampal reactivations in the hippocampal CA1 region, and may
504 serve similar plasticity mechanisms in downstream targets (*Malvache et al., 2016*). Thus,
505 dentate activity during immobility may be important to instruct downstream ensembles to

506 exhibit specific memory-related sequences. That the integrity of the dentate gyrus is
507 important in determining behaviorally relevant firing patterns in CA3 has also been
508 demonstrated by lesion experiments showing that activity of dentate GCs is necessary for
509 increased SWRs and prospective goal-directed firing of CA3 neurons (*Sasaki et al., 2018*).

510 One interesting feature of population activity in the dentate gyrus during locomotion became
511 apparent from our PCA analyses. We noted that population behavior in the dentate gyrus
512 was very dissimilar during different laps, even though animals traversed the identical belt
513 sections. A qualitatively similar finding has been obtained in a recent publication, showing
514 that even after extensive training in the very same environment on successive days, different
515 sets of dentate granule cells were activated every day (Lamothe-Molina et al., 2020, bioRxiv,
516 Doi: <https://doi.org/10.1101/2020.08.29.273391>). The population dynamics that we observed
517 in DG were very different from CA1, which expectedly shows a very robust association with
518 space during repetitive laps. One interpretation of this finding is that the dentate gyrus
519 amplifies small difference between laps, and is able to represent successive laps in a
520 different way; this itself being a potential manifestation of the pattern separation capabilities
521 of this structure. We note that while this is conceptually compelling, these experiments do not
522 prove that this is the case.

523 If network events are important in memory processes, then inhibiting dentate gyrus activity
524 during the entire period the animal is resting should impede the formation of dentate gyrus-
525 dependent memories. It would be desirable to inhibit only network events to test this idea,
526 but, due to the sparseness and high synchrony of these events, a closed loop approach to
527 achieve this is not feasible. Thus, the behavioral experiments have to be interpreted with
528 caution, as all resting activity is being inhibited, regardless of whether they constitute network
529 events or not. Inhibiting only granule cells during immobility to test the effect this has on a
530 dentate-dependent memory tasks should therefore be considered a hypothesis testing
531 experiment, but does not provide definite proof of the relevance of network events. The OPS
532 task requires storage of the initial object location with a high degree of precision that can be

533 utilized later on for discriminating the translocated object. We show that optogenetically
534 inhibiting GCs, even if this was done only during immobility remote from the explored objects,
535 disrupted the capability to acquire such memories. This supports the idea that dentate
536 network events may rapidly and flexibly introduce information about the environment into the
537 hippocampal network, in the time intervals interspersed between episodes of exploration.
538 Consistent with this view of 'real-time updating', we observed increased incorporation of
539 spatial information via place cell integration into network events upon the first experience of a
540 cue-rich environment. Inhibition of the dentate gyrus during the recall phase did not
541 significantly inhibit task performance, consistent with the idea that recall of precise location
542 information is achieved via activation of memory-related attractors in downstream CA3
543 and/or CA1 regions. Indeed, behavioral analyses combined with selective lesions of dentate
544 gyrus and CA3 have also suggested an interaction between CA3 and DG in supporting
545 encoding but not retrieval processes in a spatial learning task (*Jerman et al., 2006*).
546 Moreover, disrupting dentate spikes via electrical stimulation has been shown to disrupt
547 acquisition of hippocampal-dependent trace eyeblink conditioning (Nokia et al. 2017).

548 We also performed inhibition of dentate granule cells only during locomotion in the OPS task.
549 This inhibition also prevented the formation of spatial memories. This may simply reflect that
550 mice are not able to store the initial object location if exploratory activity is disrupted. On the
551 other hand, it is possible that the dentate gyrus is encoding the experience of the initial
552 session in the OPS task as a single sequence spanning rest and running. In this case,
553 inhibition of population at any point during the entire experience could disrupt memory
554 formation, and would not reflect a specific role of DG activity during rest.

555 Two caveats have to be considered in these behavioral experiments. First, while it is very
556 likely that network events of a similar kind occur in freely moving mice during the OPS task,
557 we have not explicitly shown this. A second caveat when using optogenetics for behavioral
558 experiments are the known aberrant effects of some opsins. Because the design of our
559 experiment involves closed-loop stimulation and requires inhibition with relatively fast
560 kinetics, we had to select a fast inhibitory opsin for these experiments, with NpHR and ArchT

561 as the most established opsins in this category. While rebound excitation effects have been
562 described for NpHR, and not for the most prominent alternative ArchT following illumination
563 (**Raimondo et al., 2012**), ArchT has pH-dependent effects in synaptic terminals, which lead
564 to very powerful, action potential independent excitation of Arch-expressing terminals during
565 illumination (**Mahn et al., 2016**). Because this could lead to aberrant excitation of hilar
566 neurons during illumination, ArchT was not a viable alternative in our experiments. We
567 therefore used NpHR as the most appropriate strategy, and utilized pulsed stimulation to
568 minimize unwanted side effects. However, we acknowledge rebound excitation effects may
569 be a potential confounding factor.

570 How do network events correspond to the different types of activity that have been described
571 in the dentate gyrus during immobility or sleep, namely dentate spikes and sharp waves
572 (Bragin et al. 1995; Penttonen et al. 1997)? During dentate spikes, granule cells are
573 discharged anterogradely by entorhinal input, while they are activated retrogradely by the
574 CA3-mossy cell feedback pathway during sharp waves (Bragin et al. 1995; Penttonen et al.
575 1997). We show that dentate network events are associated with MPP activation, but would
576 be cautious in designating these events dentate spikes in the absence of parallel in-vivo
577 electrophysiology, especially given recent descriptions of other subclasses of DG sharp
578 waves (**Meier et al., 2020**).

579 Activity in the dentate gyrus may also be relevant for processes on more extended time
580 scales, such as maintenance of established memories. For instance, pharmacogenetic
581 inhibition of GCs induces loss of a hippocampal memory in trace eyeblink conditioning
582 (**Madroñal et al., 2016**). Such longer time-scale coding may be mediated by processes that
583 extend beyond local hippocampal computations. Along these lines, dentate gyrus activity
584 during dentate spikes is associated with wide-spread increases in single-cell activity, gamma
585 oscillations and intraregional gamma coherence (**Headley et al., 2017**). It is thus possible
586 that the precise activation patterns we observe in dentate gyrus here are part of a more
587 distributed, organized activity occurring in immobile animals.

588 In summary, we described a novel form of synchronized, sparse network activity during
589 immobility in DG that is potentially relevant to the formation of dentate gyrus-dependent
590 spatial memories.

591

592 **Methods**

593 *Animals and procedures:* All animal experiments were conducted in accordance with
594 European (2010/63/EU) and federal law (TierSchG, TierSchVersV) on animal care and use
595 and approved by the county of North-Rhine Westphalia (LANUV AZ 84-02.04.2015.A524, AZ
596 81-02.04.2019.A216). We used 9-12 weeks old Thy1-GCaMP6 mouse line (GP4.12Dkim/J)
597 mice for imaging experiments, which express GCaMP6s in most hippocampal neurons
598 (*Dana et al., 2014*). For optogenetic inhibition of the dentate gyrus granule cells, we used
599 heterozygous Prox1-Cre animals (Tg(Prox1-cre)SJ39Gsat/Mmucd) obtained from MMRRC
600 UC Davis as cryopreserved sperm and rederived in the local facility.

601 *Virus injections and head fixation:* Thy1-GCaMP6 mice were anesthetized with a combination
602 of fentanyl/midazolam/medetomidine (0.05 / 5.0 / 0.5 mg/kg body weight i.p.) and head-fixed
603 in a stereotactic frame. 30 min prior to induction of anesthesia, the animals were given a
604 subcutaneous injection of ketoprofen (5 mg/kg body weight). Eyes were covered with eye-
605 ointment (Bepanthen, Bayer) to prevent drying and body temperature was maintained at
606 37°C using a regulated heating plate (TCAT-2LV, Physitemp) and a rectal thermal probe.
607 After removal of the head hair and superficial disinfection, the scalp was removed about 1
608 cm² around the middle of the skull. The surface was locally anesthetized with a drop of 10%
609 lidocaine and after 3-5 min residual soft tissue was removed from the skull bones with a
610 scraper and 3% H₂O₂/NaCl solution. After complete drying, the cranial sutures were clearly
611 visible and served as orientation for the determination of the drilling and injection sites. For
612 virus injection, a hole was carefully drilled through the skull with a dental drill, avoiding
613 excessive heating and injury to the meninges. Any minor bleeding was stopped with a sterile
614 pad. The target site was located as the joint of Parietal, Interparietal and Occipital skull
615 plates. Subsequently, the tip of a precision syringe (cannula size 34 G) was navigated
616 stereotactically through the burrhole (30° towards vertical sagittal plane, 1.5 mm depth from
617 skull surface) to target the following coordinates: Anteroposterior [AP] measured from
618 bregma ~4.6 mm; lateral [L] specified from midline ~3 mm; dorsoventral [DV] from surface of

619 the skull ~4.2 mm. Virus particles (rAAV2/1-CaMKIIa-NES-jRGECO1a (*Dana et al., 2016*))
620 were slowly injected (total volume 250 nl, 50 nl / min) in the medial entorhinal cortex. Correct
621 injection site in the medial entorhinal cortex was verified in all cases by confined expression
622 of jRGECO1a in the middle molecular layer of the dentate gyrus (**Fig. 1A**). To prevent reflux
623 of the injected fluid, the cannula was retained for 5 minutes at the injection site. Optibond
624 (Optibond™ 3FL; two component, 48% filled dental adhesive, bottle kit; Kerr; FL, USA) was
625 then applied thinly to the skull to aid adhesion of dental cement. Subsequently, a flat custom-
626 made head post ring was applied with the aid of dental cement (Tetric Evoflow), the borehole
627 was closed and the surrounding skin adapted with tissue glue, also closing the borehole and
628 adapting the surrounding skin with tissue glue. At the end of the surgery, anesthesia was
629 terminated by i.p. injection of antagonists (naloxone/flumazenil/atipamezole, 1.2 / 0.5 / 2.5
630 mg / kg body weight). Postoperative analgesia was carried out over 3 days with 1 × daily
631 ketoprofen (5 mg/kg body weight, s.c.).

632 *Window implantation procedure:* Cranial window surgery was performed to allow imaging
633 from the hippocampal dentate gyrus. 30 minutes before induction of anesthesia, the
634 analgesic buprenorphine was administered for analgesia (0.05 mg/kg body weight) and
635 dexamethasone (0.1 mg/20 g body weight) was given to inhibit inflammation. Mice were
636 anesthetized with 3-4% isoflurane in an oxygen/air mixture (25/75%) and then placed in a
637 stereotactic frame. Eyes were covered with eye-ointment (Bepanthen, Bayer) to prevent
638 drying and body temperature was maintained at 37°C using a regulated heating plate (TCAT-
639 2LV, Physitemp) and a rectal thermal probe. The further anesthesia was carried out via a
640 mask with a reduced isoflurane dose of 1-2% at a gas flow of about 0.5 l / minute. A circular
641 craniotomy (Ø 3 mm) was opened above the right hemisphere hippocampus using a dental
642 drill. Cortical and CA1 tissue was aspirated using a blunted 27-gauge needle until the blood
643 vessels above the dentate gyrus became visible. A custom-made cone-shaped silicon inset
644 (Upper diameter 3 mm, lower diameter 1.5 mm, length 2.3 mm, RTV 615, Movimentive)
645 attached to by a cover glass (Ø 5 mm, thickness 0.17 mm) was inserted and fixed with dental
646 cement. This special window design allowed easy implantation and maintenance and

647 minimized the amount of aspirated tissue. Further the geometry was optimal for conserving
648 the numerical aperture of the objective (see **Fig. 1-figure supplement 1D-F**). Postoperative
649 care included analgesia by administering buprenorphine twice daily (0.05 mg/kg body weight)
650 and ketoprofen once daily (5 mg/kg body weight s.c.) on the three consecutive days after
651 surgery. Animals were carefully monitored twice daily on the following 3 days, and recovered
652 from surgery within 24-48 hours, showing normal activity and no signs of pain. The
653 preparation of CA1 imaging windows followed mainly the same protocol. Here only the cortex
654 was aspirated until the alveus fibers above CA1 became visible. The silicon inset was shorter
655 version (length 1.5 mm) of the one used for DG experiments.

656 *Two-photon calcium imaging:* We used a commercially available two photon microscope (A1
657 MP, Nikon) equipped with a 25x long-working-distance, water-immersion objective (N.A.=1,
658 WD=4 mm, XLPLN25XSVMP2, Olympus) controlled by NIS-Elements software (Nikon).
659 GCaMP6s was excited at 940 nm using a Ti:Sapphire laser system (~60 fs laser pulse width;
660 Chameleon Vision-S, Coherent) and a fiber laser system at 1070 nm (55 fs laser pulse width,
661 Fidelity-2, Coherent) to excite jRGECO1a (see **Fig. 1-figure supplement 1B**). Emitted
662 photons were collected using gated GaAsP photomultipliers (H11706-40, Hamamatsu).
663 Movies were recorded using a resonant scanning system at a frame rate of 15 Hz and
664 duration of 20 minutes per movie.

665 *Habituation and behavior on the linear track:* Experiments were performed in head fixed
666 awake mice running on a linear track. Two weeks before the measurements, mice were
667 habituated to the head fixation. Initially mice were placed on the treadmill without fixation for
668 5 minutes at a time. Subsequently, mice were head-fixed, but immediately removed if signs
669 of fear or anxiety were observed. These habituation sessions lasted 5 minutes each and
670 were carried out three times per day, flanked by 5 minutes of handling. During the following
671 3-5 days, sessions were extended to 10 minutes each. The duration of sessions used for
672 experiments was always 20 minutes each. After habituation, mice ran well on the treadmill
673 for average distances between 30 and 40 meters per session (see **Fig. 1-figure supplement**

674 **1H**). The treadmill we implemented was a self-constructed linear horizontal treadmill, similar
675 to (**Royer et al., 2012**). Three different belt configurations were used. In the first, no spatial
676 cues were added to the belt beyond the texture of the belt itself (baseline condition). Three
677 twenty-minute sessions were carried out for each mouse on consecutive days. In the second,
678 cue enriched condition, the belt surface was equipped with tactile cues (see **Fig. 1-figure**
679 **supplement 1G**). In the zone condition the belt was divided in three zones where each zone
680 contained unique tactile cues. Belt position and running speed were measured by modified
681 optical computer-mouse sensors. All stimulation and acquisition processes were controlled
682 by custom-made software written in LabView (**Source Code File 1**).

683 *Pupil diameter measurement and analysis:* On the linear track, the pupil diameter was
684 measured using a high-speed camera (Basler Pilot, Basler, Germany) at a framerate of 100
685 Hz. To estimate pupil diameter, a circular shape was fitted to the pupil using the LabView NI
686 Vision toolbox (National Instruments), providing a real-time readout. Post-hoc, the pupil-
687 diameter trace was normalized to its mean. As in a published study (**Reimer et al., 2014**),
688 frames in which pupil diameters could not be obtained due to blinking or saccades were
689 removed from the trace. The pupil diameter trace was filtered using a Butterworth low-pass
690 filter at a cutoff frequency of 4 Hz. To match the time resolution of the imaging data, the
691 pupil-trace was down-sampled to 15 Hz. Average pupil diameters were calculated for entire
692 episodes of locomotion, entire periods of immobility, and for the single frame coincident with
693 the peak of granule cell activity during network events.

694 *Data analysis, 2-photon imaging:* All analysis on imaging data and treadmill behavior data
695 were conducted in MATLAB using standard toolboxes, open access toolboxes and custom
696 written code. To remove motion artifacts, recorded movies were registered using a Lucas–
697 Kanade model (**Greenberg and Kerr, 2009**). Individual cell locations and fluorescence
698 traces were identified using a constrained nonnegative matrix factorization based algorithm
699 and afterwards Ca^{2+} events were identified with a constrained deconvolution algorithm
700 (**Pnevmatikakis et al., 2016**). All components were manually inspected and only those that

701 showed shape and size of a granular cell and at least one Ca^{2+} -event amplitude three
702 standard deviations above noise level in their extracted fluorescence trace were kept. We
703 binarized individual cell fluorescence traces by converting the onsets of detected Ca^{2+} events
704 to binary activity events. We did not observe any indication of epileptiform activity in Thy1-
705 GCaMP6 (GP4.12Dkim/J) mice, in line with previous work (**Steinmetz et al., 2017**). On
706 average 5-6% of the GC population was active during synchronized network events (Mean:
707 5,71 %, Median: 5.03%, n = 1312 NEs, 9 mice, 3 sessions).

708 *Analysis of MPP input signals:* MPP input bulk signal was analyzed by setting a region of
709 interest in the molecular layer. For that, a threshold of 50 % maximum fluorescence was
710 used within the field of view on the average projection of the movie. The bulk fluorescence
711 signal trace was calculated as the average signal of the defined region of interest in each
712 frame. The baseline for the bulk signal was defined as the low pass filtered signal of the raw
713 trace with a cutoff frequency of 0.01 Hz using a Butterworth filter model. We used a
714 constrained deconvolution algorithm (**Pnevmatikakis et al., 2016**) to create a proxy for the
715 underlying activity of the bulk signal. This allowed for identification of precise onset times and
716 normalized amplitude values of Ca^{2+} events in MPP input data.

717 *Network activity:* To define events of synchronized activity we used binarized data that
718 marked the onset of each significant Ca^{2+} -event. First, we searched for events occurring
719 simultaneously in several GCs within a moving time window of 200ms which corresponds to
720 1 ± 1 frames in our recordings, where multiple events in one cell were counted as one. We
721 then defined the distribution of synchronous events that could arise by chance in each
722 individual session using three different shuffling approaches. Firstly, for every individual cell
723 the event onset times were redistributed to random times, thereby conserving the mean
724 event frequency per cell but destroying temporal correlations. This was done for every cell
725 and repeated a thousand times to create a null-distribution of population behavior. To
726 ascertain how robustly the data were different from the null distribution, we identified the
727 number of synchronous events for different network event size thresholds (See **Fig. 1-figure**

728 **supplement 3A** for average values, green line real data, grey line shuffled data, see **Fig. 1-**
729 **figure supplement 3D-I** for six individual representative examples). The second shuffling
730 approach shifted complete traces of onset times with respect to each other. This maintains
731 within-cell correlations of firing (i.e. episodes of higher frequency firing), but reduces
732 between-cell correlations. This is shown in **Fig. 1-figure supplement 3B** (averages, green
733 line real data, red line shuffled data). In the representative examples in **Fig. 1-figure**
734 **supplement 3D-I**, this shuffling approach is shown as red lines in the rightmost panels (note
735 that the three shuffling curves are closely superimposed). The third shuffling approach
736 considers potential differences of individual cell activity levels during locomotion and
737 immobility. To account for this, event onset times were randomly re-distributed only within
738 these activity states (**Fig. 1-figure supplement 3C** for averages green line real data, purple
739 line shuffled data, **Fig. 1-figure supplement 3D-I**, this shuffling method shown as purple line
740 in rightmost panels). All three shuffling methods reveal that significantly more synchrony is
741 observed than expected by chance. We then set the minimal threshold for network events in
742 each individual session at that number of synchronously active granule cells where less than
743 0.1% of events ($p < 0.001$) could be explained by chance.

744 Orthogonality between pairs of network events was assessed using cosine-similarity
745 measures. To this end, population vectors of all network events derived from binarized data
746 were multiplied using the normalized vector-product in a pair-wise manner. To test which
747 fraction of orthogonal pairs could be explained by chance, we generated a null distribution by
748 randomly reassigning the cell participations to different population vectors a 1000 times. We
749 then tested the real fraction of orthogonal pairs against the fraction derived from the shuffled
750 data (**Source Code File 2, 3**).

751 *Spatial tuning*: To assess spatial tuning of activity in sparsely coding GCs we used spatial
752 tuning vector analysis (*Danielson et al., 2016*). We restricted analysis to running epochs,
753 where a running epoch was defined as an episode of movement with a minimal duration of
754 2.5 s above a threshold of 4 cm/s in a forward direction. The threshold of 4cm/s was chosen

755 in line with both literature using head-fixed mice (i.e. (**Danielson et al., 2016**)), as well as a
756 very extensive literature in freely moving animals (i.e. (**Kay et al., 2016**)). Only cells with 4 or
757 more event onsets during running epochs were included in the analysis. We used binarized
758 data to calculate the mean of the vectors pointing in the mouse position at the times of
759 transient onsets, weighted by the time spent in that bin. We addressed statistical significance
760 by creating the null distribution for every spatially tuned cell. This was achieved by randomly
761 shuffling the onset times and recalculating the spatial tuning vector 1000 times. The p value
762 was calculated as the percentage of vector lengths arising from the shuffled distribution that
763 was larger than the actual vector length.

764 *Velocity tuning:* To analyze speed modulated activity of GCs, velocity values were divided in
765 20 evenly sized bins between 0 and the maximum velocity of the animal. We calculated the
766 mean $\Delta F/F$ at all times the animal was running at velocities within each specific velocity bin.
767 Putative speed cells were those granule cells that showed a Pearson's r of at least 0.9. To
768 further exclude the possibility that correlations arise by chance we shifted the individual $\Delta F/F$
769 traces with respect to the behavior randomly in the time domain 1000 times. The cell was
770 considered a significant speed coder if the shuffle-data r-values were below the original one
771 in at least 95 % of the cases.

772 *Hierarchical cluster analysis:* To find ensembles of correlated activity within network activity,
773 we focused only on those granule cell Ca^{2+} events that occurred within network events. We
774 calculated the correlation matrix from binarized data using Pearson's r for all cell
775 combinations. To identify clusters of correlated cells we used agglomerative hierarchical
776 cluster trees. Clusters were combined using a standardized Euclidean distance metric and a
777 weighted average linkage method. Clusters were combined until the mean of the cluster
778 internal r-value reached a significance threshold. To define the significance threshold, we
779 created a null-distribution of r-values from randomized data sets. Data was shuffled by
780 randomly reassigning all network related events to different network events for every cell.
781 This process was repeated 1000 times and the 95 percentiles of the created r-value null-

782 distribution was used as the threshold for the clustering procedure. Only clusters in which the
783 mean intra-cluster r-value exceeded the threshold obtained from the null distribution were
784 considered for further analysis (see **Source Code File 4**).

785 *Principal Component Analysis:* To perform Principal Component Analysis (PCA) and
786 Independent Component Analysis (ICA) we used standard MATLAB procedures and
787 calculated the maximal number of components. Gaussian Process Factor Analysis (GPFA)
788 was conducted using a formerly described procedure and toolbox (*Yu et al., 2009*), that we
789 adapted for Ca^{2+} -imaging data. Principals were calculated using singular value
790 decomposition (SVD) of the data \mathbf{X} of size N by T , where N is the number of cells, T the
791 number of recorded frames and the rows of \mathbf{X} are the z-scored $\Delta F/F$ traces, decomposing
792 the data-matrix as

$$\mathbf{X} = \mathbf{V}\mathbf{W}$$

793 where \mathbf{V} is an orthogonal matrix whose columns are the principal components, and \mathbf{W} is a
794 matrix of associated weights. For an analysis of population activity patterns relative to spatial
795 location, we projected the animal position onto PCA trajectories, allowing us to identify loops
796 in component space reflecting complete laps on the belt. Further we projected all individual
797 component amplitudes onto the position of the mouse to detect repetitive patterns. This
798 analysis had comparable results for PCA, as well as ICA and GPFA (**Fig. 7-figure**
799 **supplement 1A-C** for dentate gyrus, **D-F** for CA1).

800 *Analysis of spatial representation using PCA weights:* After performing PCA we quantified
801 spatial representation within our data using the weights \mathbf{W}_{run} . To that end we projected the
802 amplitudes of \mathbf{W}_{run} of the five first components onto the linear space defined by the 150 cm
803 linear track. Spatial tuning leads to a harmonic behavior of amplitudes with respect to mouse
804 position (see **Fig. 7-figure supplement 2E-H**) and the periodicity was quantified using the
805 normalized autocorrelation of each weight. In the individual examples (see **Fig. 7-figure**
806 **supplement 2I-L**) as well as averaged over animals (see **Fig. 7-figure supplement 2M-P**),
807 peaks in the autocorrelation were observed at integer multiples of rounds, in particular in

808 CA1. To compare the strength of spatial tuning in different DG-experimental conditions as
809 well as CA1 data we quantified and averaged the peak values at a delay of one round (see
810 **Fig. 7D**).

811 *PCA-based comparison of population activity during running and immobility epochs:* For
812 further analysis, we restricted the number of components so that 50 % of variance in each
813 individual data set was explained. To compare running and network related epochs we
814 calculated principal components \mathbf{V}_{run} and \mathbf{V}_{net} independently from each other so that

$$\mathbf{X}_{\text{run}} \approx \mathbf{V}_{\text{run}} \mathbf{W}_{\text{run}}, \quad \mathbf{X}_{\text{net}} \approx \mathbf{V}_{\text{net}} \mathbf{W}_{\text{net}}$$

815 , where \mathbf{X}_{run} contains all the data from epochs of running and \mathbf{X}_{net} the data from 2 s
816 windows around all network events. To calculate the similarity between these two bases, the
817 covariance of \mathbf{X}_{run} was projected into the principal space of the network activity

$$\mathbf{S}_{\text{net} \times \text{run}} \approx \mathbf{V}_{\text{net}}^T \text{COV}(\mathbf{X}_{\text{run}}) \mathbf{V}_{\text{net}}$$

818 , where $\mathbf{S}_{\text{net} \times \text{run}}$ is the matrix of projected co-variances and $\text{trace}(\mathbf{S}_{\text{net} \times \text{run}})$ quantifies the
819 amount of projected co-variance. This number was normalized to the total amount of
820 covariance of locomotion activity in the locomotion principal space $\text{trace}(\mathbf{S}_{\text{run} \times \text{run}})$.

821 To compare our results against chance level, we used three different shuffling approaches to
822 exclude possible mechanisms for similarities that could arise by chance. In the first
823 procedure we used the entire traces recorded during immobility, randomly shift those with
824 respect to each other in the time domain. This approach conserved individual activity levels
825 and intra-neuronal correlations while creating randomized inter-neuronal correlations. We
826 applied the original network times to these time shifted traces to create a random principal
827 direction space \mathbf{V}_{rand} and calculated the projected co-variances of \mathbf{X}_{run} into the random-
828 network space as $\text{trace}(\mathbf{S}_{\text{rand} \times \text{run}})$. For shuffling approaches two and three, we shuffled within
829 the matrix of concatenated NEs – in other words, only the 2 seconds around NEs rather than
830 the entire time-series used in shuffle one. For the second approach we tested if the

831 composition of individual NEs is important. To this end, for each individual NE, we randomly
832 reassigned activity of a given cells activity to a different cell. Thus, NEs have exactly the
833 same number of active cells, but the identity of cells active within them has been randomly
834 changed, and the number of NEs that individual cells participate in will be altered. In the third
835 shuffling method we tested whether similarity could be driven by the activity level of individual
836 cells within NEs. Therefore, we randomly reassigned each cells' NE activity to other NEs.
837 This approach maintains the number of NEs a given cell participates and randomizes the
838 interactions between specific sets of cells. All procedures were repeated 1000 times and the
839 p-value was calculated as the percentage of random projections that exceeded the initial
840 value.

841 Additionally, we used two alternative approaches to quantify similarity between the PCA
842 bases. First a similarity factor S_{PCA} as described by Krzanowski (**Krzanowski, 1979**).

$$S_{\text{PCA}} = \text{trace}(\mathbf{V}_{\text{net}}^T \mathbf{V}_{\text{run}} \mathbf{V}_{\text{run}}^T \mathbf{V}_{\text{net}}) = \sum_{i=1}^k \cos^2 \theta_i$$

843 , where θ_i is the angle between the i 'th principal directions of \mathbf{V}_{run} and \mathbf{V}_{net} . Further the
844 Eros similarity factor as described in (**Yang, K., Shahabi, C., 2004**) was used:

$$\text{Eros} = \sum_{i=1}^k w_i |\cos \theta_i|$$

845 where w_i is a weighting factor. All measures delivered comparable results as compared to
846 shuffled data. All different procedures of similarity calculation and shuffling available with this
847 paper (see **Source Code File 5**).

848 *In-vitro patch-clamp experiments:* Acute slices were prepared from mice expressing NpHR-
849 eYFP in GCs. NpHR expression was induced by rAAV mediated gene transfer (rAAV2/1-
850 DOI-eNpHR3-eYFP) into Prox1-Cre mice (see below for virus injection protocols). >2 weeks
851 after virus injection, animals were deeply anesthetized with Isoflurane (Abbott Laboratories,
852 Abbot Park, USA) and decapitated. The head was instantaneously submerged in ice-cold

853 carbogen saturated artificial cerebrospinal fluid (containing in mM: NaCl, 60; sucrose, 100;
854 KCl, 2.5; NaH₂PO₄, 1.25; NaHCO₃, 26; CaCl₂, 1; MgCl₂, 5; glucose, 20) and the brain
855 removed. Horizontal 350 μm thick sections were cut with a vibratome (VT1200 S, Leica,
856 Wetzlar, Germany). Slices were incubated at 35 °C for 20 to 40 minutes and then stored in
857 normal ACSF (containing in mM: NaCl, 125; KCl, 3.5; NaH₂PO₄, 1.25; NaHCO₃, 26; CaCl₂,
858 2.0; MgCl₂, 2.0; glucose, 15) at room temperature. Recordings were performed in a
859 submerged recording chamber at 33- 35 °C under constant superfusion with carbogen
860 saturated ACSF (3 ml/min). Visually identified GCs were recorded in current clamp using a
861 low chloride intracellular solution (containing in mM: K-gluconate, 140; 4-(2-hydroxyethyl)-1-
862 piperazineethanesulfonic acid (HEPES-acid), 5; ethylene glycol tetraacetic acid (EGTA),
863 0.16; MgCl₂, 0.5; sodium phosphocreatine, 5) and a Multiclamp 700B and Digidata 1322A
864 (Molecular Devices). Illumination (~560nm, ~1mW) was achieved through the Objective.
865 Action potential frequencies were calculated using the smallest current injection yielding at
866 least 4 action potentials.

867 *Light fiber implantation for behavioral experiments:* Mice were injected with buprenorphine
868 (0.05 mg/kg BW) 30 minutes before inducing anesthesia using 3.5 % isoflurane for induction
869 and 1-1.5 % for maintenance. Mice were placed in a stereotactic frame (Kopf Instruments)
870 and the scalp opened with surgical scissors after disinfecting it with iodine solution and
871 applying local anesthetic (10% lidocaine). The skull was thoroughly cleaned using 2% H₂O₂,
872 covered with a thin layer of two-component dental adhesive (Optibond) and the surrounding
873 wound sealed with tissue glue (Vetbond). Small craniotomies were performed above the
874 target sites and 500 nl virus suspension (rAAV2/1-Ef1a-DOI-NLS-eYFP for controls,
875 rAAV2/1-EF1a-DOI-eNpHR3-eYFP for experimental group) was bilaterally injected using a
876 34 G syringe (Nanofill Syringe, World Precision Instruments, Inc.) at a speed of 50 nl/min.
877 After each injection, the syringe was kept in place for 5 minutes to ensure permeation of the
878 virus into the parenchyma. Coordinates for viral injections into dorsal dentate gyrus were:
879 (from bregma): AP: -2.3; ML: -/+ 1.6 and DV: 2.5 mm). Afterwards, fiber optic cannulae of
880 200 μm diameter (NA: 0.39, CFMLC12, Thorlabs) were bilaterally implanted at (from

881 bregma): AP: -1.7; ML: +/- 1.35 and DV: 1.7 and fixed to the skull with a layer of flowable
882 opaque composite (Tetric Evoflow) topped by multiple layers of dental cement (Paladur,
883 Heraeus). Finally, antibiotic cream (Refobacin, Almirall) was applied to the wound and the
884 animals received ketoprofen (5 mg/kg BW) s. c. Analgesia was applied post-surgery by
885 injecting ketoprofen (5 mg/kg BW) s. c. after 24, 48, and 72 hours. All mice recovered for at
886 least 3 weeks after surgery before the start of behavioral experiments.

887 *Behavioral experiments.* To test the effect of optogenetic inhibition of granule cells, 23
888 heterozygous Prox1-Cre animals (5 male, 18 female) between the age of 4 and 9 months
889 were used. Males were single caged and females were group-caged (2-4 individuals per
890 cage) in standard mouse cages under an inverted light-dark cycle with lights on at 8 pm and
891 ad libitum access to food and water. Prior to experiments, animals were randomly assigned
892 to the control or experimental group. All experiments were conducted during the dark phase
893 of the animals. Prior to experiments, mice were handled by the experimenter for at least 5
894 days (at least 5 min/day). On experimental days, animals were transported in their home
895 cages from the holding facility to the experimental room and left to habituate for at least 45
896 minutes. All experiments were performed under dim light conditions of around 20 Lux.
897 Animals were also habituated to the procedure of photostimulation by attaching a dual patch
898 cord for around 10 minutes to the bilaterally implanted light fibers and letting them run in their
899 home cage on multiple days.

900 For optogenetic stimulation, 561 nm laser light (OBIS/LS FP, Coherent, Santa Clara, CA)
901 was delivered bilaterally into the implanted optical fibers using a dual patch cord (NA: 0.37,
902 Doric lenses, Quebec, Canada) and a rotary joint (FRJ, Doric lenses, Quebec, Canada)
903 located above the behavioral test arena. The laser power was set to 5 mW at the tip of the
904 fiber probes.

905 We used a pulsed laser light at 20 Hz with a 50% duty cycle instead of continuous
906 illumination to keep the light-induced heat effect minimal in the brain. Previous studies have
907 shown that continuous light delivery to brain tissues can cause a temperature increase of up

908 to 2°C (*Owen et al., 2019*). It has been reported that changes in temperature can alter
909 neuronal physiology of rodents (*Stujenske et al., 2015*) and birds (*Long and Fee, 2008*).
910 We simulated the light-induced heat effect using the model developed by (*Stujenske et al.,*
911 *2015*). We first examined the continuous light photostimulation of 561 nm light with 5 mW
912 output power. The temperature increase reached a steady-state and was found to be 0.7°C
913 in 60 seconds. For the pulsed light stimulation used in this study, the temperature change did
914 not exceed 0.3°C in 60 seconds (see **Fig. 8-figure supplement 1K-M**). Both pulsed and
915 continuous stimulation resulted in efficient silencing of granule cell activity (**Fig. 8-figure**
916 **supplement 1F-J**). The average illumination times were not significantly different between
917 eNpHR and eYFP control groups in any of the experiments. To apply photostimulation only
918 during immobility, we used a closed loop system employing EthoVision 8.5 that opened an
919 optical shutter (SH05, Thorlabs) in the light path of the laser via a TTL pulse only when the
920 tracking software detected that the body center of the animal was moving less than 5 cm/s
921 and closed the shutter if the speed exceeded 5 cm/s over a period of 0.5 seconds. Behavior
922 was recorded using EthoVision 8.5 software (Noldus, Netherlands) and an IR camera with a
923 frame rate of 24 Hz. Videos were stored on a computer for offline analysis. To apply
924 photostimulation only during mobility, we reversed the parameters and let the shutter open
925 when the speed of the animal exceeded 5 cm/s and closed the shutter at speeds of below 5
926 cm/s for more than 0.5 seconds.

927 *Object pattern separation task:* We used the object location memory test as a test for spatial
928 learning ability. We used a circular arena (diameter: 45 cm) made of red Plexiglas with 40 cm
929 high walls as described in (*van Goethem et al., 2018*). Two pairs of almost identical building
930 blocks (4 x 3 x 7 cm) made of either plastic or metal were used as objects. All building blocks
931 were topped with a little plastic cone to prevent animals from climbing onto the objects. To
932 habituate animals to the arena and the experimental procedure, they were taken out of their
933 home cage and placed into an empty cage only with bedding for five minutes in order to
934 increase their exploration time. After connecting the mice to the photostimulation apparatus
935 via the light fiber, they were placed into the empty arena for 10 minutes with no laser light.

936 On test days, mice were again first placed into a new empty cage for 5 minutes, then
937 connected to the photostimulation apparatus and placed into the arena for 5 minutes. The
938 arena contained two identical objects placed in the middle of the arena with an inter-object
939 distance of 18 cm. The animals were allowed to freely explore the arena and the objects.
940 After 5 minutes, the animals were transferred into their home cage for 85 minutes. For the
941 recall trial, everything was done identically to the previous acquisition trial, but one of the two
942 previously encountered objects was displaced. Experiments for individual displacement
943 configuration were repeated in some cases up to three times with an interval of two days and
944 the discrimination indices averaged. The following variants of this task regarding object
945 displacement were performed using a first batch of up to 18 mice (3 males, 15 females). In a
946 first set of experiments, variable displacements (3, 6, 9 and 12 cm) were used, with inhibition
947 of granule cells carried out during the entire acquisition and recall trial (schematic in **Fig. 8-**
948 **figure supplement 1A-C**). In a second set of experiments a fixed, intermediate degree of
949 displacement (9 cm, position 3 in **Fig. 8-figure supplement 1C**) was used, and inhibition of
950 granule cells was carried out only during quiet immobility using a closed-loop system (see
951 above) in either only the acquisition trials (**Fig. 8**) or only the recall trials (**Fig. 8-figure**
952 **supplement 3**). In a final set of experiments with those mice, we applied photostimulation in
953 the acquisition trials only when the mouse was in quiet immobility and the nose point of the
954 mouse at least 4 cm away from the objects (**Fig. 8-figure supplement 3**). Lastly, with a
955 separate batch of mice consisting of 2 males and 3 females, all bilaterally injected into the
956 dentate gyrus with eNpHR-eYFP, we performed the pattern separation task with an object
957 displacement of 9 cm either without illumination, with illumination at speeds below 5 cm/s or
958 at speeds above 5 cm/s, both times in the acquisition trials (**Fig. 8-figure supplement 2**).
959 After each mouse, the arena and the objects were cleaned with 70% ethanol. An
960 experienced observer blinded to the experimental group of the animals manually scored the
961 time the animals explored the displaced and the non-displaced object by sniffing with the
962 snout in very close proximity to the objects and their head oriented towards them. We
963 calculated the discrimination index based on the following formula: (time exploring displaced

964 object – time exploring the non-displaced object) / (time exploring displaced object + time
965 exploring the non-displaced object). Trials in which the total exploration time in an acquisition
966 or recall trial was lower than 4 seconds were excluded from further analysis. Trajectory maps
967 and occupancy plots were generated using custom-written MATLAB Scripts.

968 *Histology and microscopy:* To verify successful viral transduction and window position,
969 animals were deeply anesthetized with ketamine (80 mg/kg body weight) and xylazine (15
970 mg/kg body weight). After confirming a sufficient depth of anesthesia, mice were heart-
971 perfused with cold phosphate buffered saline (PBS) followed by 4% formalin in PBS. Animals
972 were decapitated and the brain removed and stored in 4% formalin in PBS solution. Fifty to
973 70 µm thick coronal slices of the hippocampus were cut on a vibratome (Leica). For nuclear
974 staining, brain slices were kept for 10 min in a 1:1000 DAPI solution at room temperature.
975 Brain slices were mounted and the red, green and blue channel successively imaged under
976 an epi fluorescence or spinning disc microscope (Visitron VisiScope). In optogenetic
977 inhibition experiments, post-hoc microscopy was used to confirm successful expression of
978 NpHR-eYFP. Of the animals used, 3 control animals showed no eYFP expression and one
979 experimental animal lacked NpHR-eYFP expression. The animal lacking NpHR expression
980 was excluded from the study. Control animals lacking eYFP expression were assumed to
981 lack modulation of granule cell activity by illumination and were pooled with eYFP expressing
982 control animals.

983 Expression of NpHR was highly selective to the dentate gyrus, as described previously
984 (**Braganza et al., 2020; Truman et al., 2012**), and as reported in the Gensat project
985 (http://www.gensat.org/ShowMMRRCStock.jsp?mmrc_id=MMRRC:036632). Functional
986 evidence has excluded recombination in hilar interneurons in this mouse line (**Braganza et**
987 **al., 2020**). Crossing the Prox1-Cre mouse line used in the present study with a mouse
988 leading to Cre-dependent expression of ChR2 showed a lack of monosynaptic inhibitory
989 responses, as would be expected if ChR2 were also present in hilar interneurons.

990 **Acknowledgements:** We are very grateful to David Greenberg, Jason Kerr, and Damian
991 Wallace for technical help and advice, as well as the supply of analysis algorithms. We
992 gratefully acknowledge the support of Jonathan Ewell in editing the manuscript, and Antoine
993 Madar for helpful comments on an earlier manuscript draft. We acknowledge the support of
994 the Imaging Core Facility of the Bonn Technology Campus Life Sciences. The work was
995 supported by the SFB 1089, Project C04 to HB, the Research Group FOR2715, the
996 Research Priority Program SPP Computational Connectomics and EXC 2151 under
997 Germanys Excellence Strategy of the Deutsche Forschungsgemeinschaft (DFG, German
998 Research Foundation) to HB and to JHM (EXC 2064/1 PN 390727645), support of the
999 Humboldt Foundation PSI to KG, and support of the Volkswagen Foundation to LAE. ANH
1000 was supported by the IMPRS Brain and Behavior.

1001 **Competing interests:** The authors declare no competing interests.

1002

References

- 1004 **Berron D**, Schütze H, Maass A, Cardenas-Blanco A, Kuijff HJ, Kumaran D, Düzel E. 2016. Strong
1005 Evidence for Pattern Separation in Human Dentate Gyrus **36**:7569–7579.
1006 doi: 10.1523/JNEUROSCI.0518-16.2016.
- 1007 **Braganza O**, Mueller-Komorowska D, Kelly T, Beck H. 2020. Quantitative properties of a feedback
1008 circuit predict frequency-dependent pattern separation. *eLife* **9**. doi: 10.7554/eLife.53148.
- 1009 **Bragin A**, Jandó G, Nádasdy Z, van Landeghem M, Buzsáki G. 1995. Dentate EEG spikes and
1010 associated interneuronal population bursts in the hippocampal hilar region of the rat. *Journal of*
1011 *Neurophysiology* **73**:1691–1705. doi: 10.1152/jn.1995.73.4.1691.
- 1012 **Cayco-Gajic NA**, Silver RA. 2019. Re-evaluating Circuit Mechanisms Underlying Pattern Separation.
1013 *Neuron* **101**:584–602. doi: 10.1016/j.neuron.2019.01.044.
- 1014 **Dana H**, Chen TW, Hu A, Shields BC, Guo C, Looger LL, Kim DS, Svoboda K. 2014. Thy1-GCaMP6
1015 transgenic mice for neuronal population imaging in vivo **9**:e108697.
- 1016 **Dana H**, Mohar B, Sun Y, Narayan S, Gordus A, Hasseman JP, Tsegaye G, Holt GT, Hu A, Walpita D,
1017 Patel R, Macklin JJ, Bargmann CI, Ahrens MB, Schreiter ER, Jayaraman V, Looger LL, Svoboda K, Kim
1018 DS. 2016. Sensitive red protein calcium indicators for imaging neural activity. *eLife* **5**.
1019 doi: 10.7554/eLife.12727.
- 1020 **Danielson NB**, Kaifosh P, Zaremba JD, Lovett-Barron M, Tsai J, Denny CA, Balough EM, Goldberg AR,
1021 Drew LJ, Hen R, Losonczy A, Kheirbek MA. 2016. Distinct Contribution of Adult-Born Hippocampal
1022 Granule Cells to Context Encoding. *Neuron* **90**:101–112. doi: 10.1016/j.neuron.2016.02.019.
- 1023 **Davidson TJ**, Kloosterman F, Wilson MA. 2009. Hippocampal replay of extended experience. *Neuron*
1024 **63**:497–507. doi: 10.1016/j.neuron.2009.07.027.
- 1025 **Diba K**, Buzsáki G. 2007. Forward and reverse hippocampal place-cell sequences during ripples
1026 **10**:1241–1242. doi: 10.1038/nn1961.
- 1027 **Dupret D**, O'Neill J, Pleydell-Bouverie B, Csicsvari J. 2010. The reorganization and reactivation of
1028 hippocampal maps predict spatial memory performance **13**:995–1002.
- 1029 **Foster DJ**, Wilson MA. 2006. Reverse replay of behavioural sequences in hippocampal place cells
1030 during the awake state **440**:680–683. doi: 10.1038/nature04587.
- 1031 **Girardeau G**, Benchenane K, Wiener SI, Buzsáki G, Zugaro MB. 2009. Selective suppression of
1032 hippocampal ripples impairs spatial memory **12**:1222–1223. doi: 10.1038/nn.2384.
- 1033 **GoodSmith D**, Chen X, Wang C, Kim SH, Song H, Burgalossi A, Christian KM, Knierim JJ. 2017. Spatial
1034 Representations of Granule Cells and Mossy Cells of the Dentate Gyrus. *Neuron* **93**:677–690.e5.
1035 doi: 10.1016/j.neuron.2016.12.026.
- 1036 **GoodSmith D**, Lee H, Neunuebel JP, Song H, Knierim JJ. 2019. Dentate gyrus mossy cells share a role
1037 in pattern separation with dentate granule cells and proximal CA3 pyramidal cells.
1038 doi: 10.1523/JNEUROSCI.0940-19.2019.
- 1039 **Gradinaru V**, Thompson KR, Deisseroth K. 2008. eNpHR: A Natronomonas halorhodopsin enhanced
1040 for optogenetic applications **36**:129–139.
- 1041 **Greenberg DS**, Kerr JND. 2009. Automated correction of fast motion artifacts for two-photon imaging
1042 of awake animals **176**:1–15. doi: 10.1016/j.jneumeth.2008.08.020.
- 1043 **Hainmueller T**, Bartos M. 2018. Parallel emergence of stable and dynamic memory engrams in the
1044 hippocampus **558**:292–296. doi: 10.1038/s41586-018-0191-2.
- 1045 **Headley DB**, Kanta V, Paré D. 2017. Intra- and interregional cortical interactions related to sharp-
1046 wave ripples and dentate spikes **117**:556–565. doi: 10.1152/jn.00644.2016.

1047 **Jerman T**, Kesner RP, Hunsaker MR. 2006. Disconnection analysis of CA3 and DG in mediating
1048 encoding but not retrieval in a spatial maze learning task **13**:458–464. doi: 10.1101/lm.246906.

1049 **Kay K**, Sosa M, Chung JE, Karlsson MP, Larkin MC, Frank LM. 2016. A hippocampal network for spatial
1050 coding during immobility and sleep **531**:185–190. doi: 10.1038/nature17144.

1051 **Krzanowski WJ**. 1979. Between-Groups Comparison of Principal Components. *Journal of the*
1052 *American Statistical Association* **74**:703–707. doi: 10.2307/2286995.

1053 **Leutgeb JK**, Leutgeb S, Moser MB, Moser EI. 2007. Pattern separation in the dentate gyrus and CA3
1054 of the hippocampus **315**:961–966.

1055 **Long MA**, Fee MS. 2008. Using temperature to analyse temporal dynamics in the songbird motor
1056 pathway **456**:189–194. doi: 10.1038/nature07448.

1057 **Madroñal N**, Delgado-García JM, Fernández-Guizán A, Chatterjee J, Köhn M, Mattucci C, Jain A,
1058 Tsetsenis T, Illarionova A, Grinevich V, Gross CT, Gruart A. 2016. Rapid erasure of hippocampal
1059 memory following inhibition of dentate gyrus granule cells. *Nature communications* **7**:10923.
1060 doi: 10.1038/ncomms10923.

1061 **Mahn M**, Prigge M, Ron S, Levy R, Yizhar O. 2016. Biophysical constraints of optogenetic inhibition at
1062 presynaptic terminals **19**:554–556. doi: 10.1038/nn.4266.

1063 **Malvache A**, Reichinnek S, Villette V, Haimerl C, Cossart R. 2016. Awake hippocampal reactivations
1064 project onto orthogonal neuronal assemblies **353**:1280–1283. doi: 10.1126/science.aaf3319.

1065 **McGinley MJ**, David SV, McCormick DA. 2015. Cortical Membrane Potential Signature of Optimal
1066 States for Sensory Signal Detection. *Neuron* **87**:179–192. doi: 10.1016/j.neuron.2015.05.038.

1067 **Meier K**, Merseburg A, Isbrandt D, Marguet SL, Morellini F. 2020. Dentate Gyrus Sharp Waves, a
1068 Local Field Potential Correlate of Learning in the Dentate Gyrus of Mice **40**:7105–7118.
1069 doi: 10.1523/JNEUROSCI.2275-19.2020.

1070 **Neunuebel JP**, Knierim JJ. 2012. Spatial firing correlates of physiologically distinct cell types of the rat
1071 dentate gyrus **32**:3848–3858. doi: 10.1523/JNEUROSCI.6038-11.2012.

1072 **O'Reilly RC**, McClelland JL. 1994. Hippocampal conjunctive encoding, storage, and recall: Avoiding a
1073 trade-off **4**:661–682. doi: 10.1002/hipo.450040605.

1074 **Owen SF**, Liu MH, Kreitzer AC. 2019. Thermal constraints on in vivo optogenetic manipulations
1075 **22**:1061–1065. doi: 10.1038/s41593-019-0422-3.

1076 **Penttonen M**, Kamondi A, Sik A, Acsády L, Buzsáki G. 1997. Feed-forward and feed-back activation of
1077 the dentate gyrus in vivo during dentate spikes and sharp wave bursts **7**:437–450.
1078 doi: 10.1002/(SICI)1098-1063(1997)7:4<437::AID-HIPO9>3.0.CO;2-F.

1079 **Pilz GA**, Carta S, Stauble A, Ayaz A, Jessberger S, Helmchen F. 2016. Functional Imaging of Dentate
1080 Granule Cells in the Adult Mouse Hippocampus. *Journal of Neuroscience* **36**:7407–7414.

1081 **Pnevmatikakis EA**, Soudry D, Gao Y, Machado TA, Merel J, Pfau D, Reardon T, Mu Y, Lacefield C, Yang
1082 W, Ahrens M, Bruno R, Jessell TM, Peterka DS, Yuste R, Paninski L. 2016. Simultaneous Denoising,
1083 Deconvolution, and Demixing of Calcium Imaging Data. *Neuron* **89**:285–299.
1084 doi: 10.1016/j.neuron.2015.11.037.

1085 **Raimondo JV**, Kay L, Ellender TJ, Akerman CJ. 2012. Optogenetic silencing strategies differ in their
1086 effects on inhibitory synaptic transmission **15**:1102–1104. doi: 10.1038/nn.3143.

1087 **Reimer J**, Froudarakis E, Cadwell CR, Yatsenko D, Denfield GH, Tolias AS. 2014. Pupil fluctuations
1088 track fast switching of cortical states during quiet wakefulness. *Neuron* **84**:355–362.
1089 doi: 10.1016/j.neuron.2014.09.033.

1090 **Reimer J**, McGinley MJ, Liu Y, Rodenkirch C, Wang Q, McCormick DA, Tolias AS. 2016. Pupil
1091 fluctuations track rapid changes in adrenergic and cholinergic activity in cortex. *Nature*
1092 *communications* **7**:13289. doi: 10.1038/ncomms13289.

1093 **Royer S**, Zemelman BV, Losonczy A, Kim J, Chance F, Magee JC, Buzsaki G. 2012. Control of timing,
1094 rate and bursts of hippocampal place cells by dendritic and somatic inhibition **15**:769–775.

1095 **Rubin A**, Sheintuch L, Brande-Eilat N, Pinchasof O, Rechavi Y, Geva N, Ziv Y. 2019. Revealing neural
1096 correlates of behavior without behavioral measurements **10**:4745. doi: 10.1038/s41467-019-
1097 12724-2.

1098 **Sakon JJ**, Suzuki WA. 2019. A neural signature of pattern separation in the monkey hippocampus.
1099 *Proceedings of the National Academy of Sciences of the United States of America* **116**:9634–9643.
1100 doi: 10.1073/pnas.1900804116.

1101 **Sasaki T**, Piatti VC, Hwaun E, Ahmadi S, Lisman JE, Leutgeb S, Leutgeb JK. 2018. Dentate network
1102 activity is necessary for spatial working memory by supporting CA3 sharp-wave ripple generation
1103 and prospective firing of CA3 neurons **21**:258–269. doi: 10.1038/s41593-017-0061-5.

1104 **Senzai Y**, Buzsáki G. 2017. Physiological Properties and Behavioral Correlates of Hippocampal
1105 Granule Cells and Mossy Cells. *Neuron* **93**:691-704.e5. doi: 10.1016/j.neuron.2016.12.011.

1106 **Skaggs WE**, McNaughton BL. 1996. Replay of neuronal firing sequences in rat hippocampus during
1107 sleep following spatial experience **271**:1870–1873. doi: 10.1126/science.271.5257.1870.

1108 **Stefanini F**, Kushnir L, Jimenez JC, Jennings JH, Woods NI, Stuber GD, Kheirbek MA, Hen R, Fusi S.
1109 2020. A Distributed Neural Code in the Dentate Gyrus and in CA1. *Neuron* **107**:703-716.e4.
1110 doi: 10.1016/j.neuron.2020.05.022.

1111 **Steinmetz NA**, Buetfering C, Lecoq J, Lee CR, Peters AJ, Jacobs EAK, Coen P, Ollerenshaw DR, Valley
1112 MT, Vries SEJ de, Garrett M, Zhuang J, Groblewski PA, Manavi S, Miles J, White C, Lee E, Griffin F,
1113 Larkin JD, Roll K, Cross S, Nguyen TV, Larsen R, Pendergraft J, Daigle T, Tasic B, Thompson CL,
1114 Waters J, Olsen S, Margolis DJ, Zeng H, Hausser M, Carandini M, Harris KD. 2017. Aberrant Cortical
1115 Activity in Multiple GCaMP6-Expressing Transgenic Mouse Lines. *eNeuro* **4**.
1116 doi: 10.1523/ENEURO.0207-17.2017.

1117 **Stujenske JM**, Spellman T, Gordon JA. 2015. Modeling the Spatiotemporal Dynamics of Light and
1118 Heat Propagation for In Vivo Optogenetics. *Cell reports* **12**:525–534.
1119 doi: 10.1016/j.celrep.2015.06.036.

1120 **Tibshirani R**, Walther G, Hastie T. 2001. Estimating the number of clusters in a data set via the gap
1121 statistic. *J. R. Statist. Soc. B* **63 Part 2**:411–423.

1122 **Truman LA**, Bentley KL, Smith EC, Massaro SA, Gonzalez DG, Haberman AM, Hill M, Jones D, Min W,
1123 Krause DS, Ruddle NH. 2012. ProxTom lymphatic vessel reporter mice reveal Prox1 expression in
1124 the adrenal medulla, megakaryocytes, and platelets. *The American journal of pathology* **180**:1715–
1125 1725. doi: 10.1016/j.ajpath.2011.12.026.

1126 **van Dijk MT**, Fenton AA. 2018. On How the Dentate Gyrus Contributes to Memory Discrimination.
1127 *Neuron* **98**:832-845.e5. doi: 10.1016/j.neuron.2018.04.018.

1128 **van Goethem NP**, van Hagen BTJ, Prickaerts J. 2018. Assessing spatial pattern separation in rodents
1129 using the object pattern separation task. *Nature protocols* **13**:1763–1792. doi: 10.1038/s41596-
1130 018-0013-x.

1131 **Wilson MA**, McNaughton BL. 1994. Reactivation of hippocampal ensemble memories during sleep
1132 **265**:676–679. doi: 10.1126/science.8036517.

1133 **Yang, K., Shahabi, C.** 2004. A PCA-based similarity measure for multivariate time series. *Proceedings*
1134 *of The 2nd ACM International Workshop on Multimedia Databases (MMDB)* 65–74.

1135 **Yu BM**, Cunningham JP, Santhanam G, Ryu SI, Shenoy KV, Sahani M. 2009. Gaussian-process factor
1136 analysis for low-dimensional single-trial analysis of neural population activity. *Journal of*
1137 *Neurophysiology* **102**:614–635. doi: 10.1152/jn.90941.2008.

1138

1139 **Figure captions:**

1140

1141 **Fig. 1: Synchronous dentate granule cell activations, ‘network events’, occur**
1142 **preferentially during immobility.** **A**, Expression of GCaMP6s in granule cells (Thy1-
1143 GCaMP mouse line, GP4.12Dkim/J). jRGECO was expressed in medial entorhinal cortex
1144 neurons using rAAV mediated gene transfer, and is visible in the middle molecular layer
1145 (MML) corresponding to the medial perforant path (MPP). Upper panel: Post hoc analysis in
1146 70 μm fixed slice. Nuclei stained with DAPI (blue). Lower panel: Imaging plane for
1147 simultaneous recording of MPP bulk and individual GC activity. Scale bar 100 μm . **B**, Data of
1148 representative recording session. Bulk fluorescence signal of MPP fibers (red), extracted
1149 fluorescence signals from a subset of individual GCs (black), mouse position on linear track
1150 (blue) and diameter of mouse pupil (black). **C**, Participation of granule cells in synchronous
1151 network events. Representative field of view with highlighted simultaneously active GCs.
1152 Cells active during an individual network event are depicted in the same color. A subset of
1153 neurons is active in multiple network events, recognizable as white color. **D**, Raster plot of
1154 network events. Dashed lines mark network events, corresponding to simultaneous activity of
1155 > four cells. Participating cells are highlighted according to color scheme from panel C.
1156 Running speed is depicted (blue) to distinguish running and resting periods. **E**, Fluorescence
1157 transients of participating granule cells from NEs in panel D. Color scheme corresponds to
1158 panel C and D. Each column shows all respective transients of the respective synchronous
1159 ensemble. Shown is a time window of $\pm 1\text{s}$ around each NE. Vertical scale bars correspond to
1160 100% $\Delta F/F$. **F**, Mean number of network events per twenty-minute recording session during
1161 running and resting. Network events occurred mainly during immobility (repeated measures
1162 ANOVA, $F_{(1,8)}=71.80$, $p=2\times 10^{-7}$, $n=9$ animals, 3 sessions). Grey bars depict shuffled data for
1163 each condition ($n=9$ animals). **G**, Average number of identified network events plotted
1164 against different thresholds for the size of network events in terms of numbers of
1165 synchronously active cells (green line, shaded area depicts SEM, $n=3$ mice, 3 sessions).
1166 Shuffled data null-distribution is created by randomly shuffling event times for every
1167 individual cell (grey line, shaded area depicts SEM). **H**, Frequencies of network events
1168 calculated from equal time intervals for locomotion and immobility (Repeated measures
1169 ANOVA, $F_{(1,8)} = 117.28$, $p = 2\times 10^{-6}$). **I**, Cumulative probability distribution of network event
1170 occurrence during the entire twenty-minute session for individual sessions (gray lines) and
1171 the pooled sessions (Green line, $n=9$ mice, 3 sessions). **J**, Pooled cumulative probability
1172 distribution of network event occurrence during resting periods. All resting periods of one
1173 session that were longer than 5 s were normalized to their length ($n=9$ mice, 3 sessions).

1174

1175 **Fig. 2: Granule cell and MPP activity during locomotion and immobility.** **A**, Mean MPP
1176 activity (red) and the sum of all granule cell activities (green) for a representative section of a
1177 recording session in an individual mouse. Dashed lines mark transition between resting and
1178 running periods (see blue line indicating running speed). **B**, Average MPP fluorescence and
1179 running speeds, both aligned to running onsets (dashed line). Shaded areas indicate
1180 standard error ($n=4$ mice, one mouse had only jRGECO expression in MPP, but no granule
1181 cell signal, 3 sessions per mouse). **C**, Mean fluorescence averaged during resting (dark red)
1182 and running (light red). Asterisk indicates 5 % significance threshold (repeated measures
1183 ANOVA, $F_{(1,3)} = 7,86$, $p = 0.032$, $n = 4$ mice, 3 sessions). **D**, Variance of MPP bulk signal
1184 during resting (dark red) and running (light red, $n=4$). Asterisk indicates results of repeated
1185 measures ANOVA, $F_{(1,3)} = 7,07$, $p = 0.037$, $n = 4$ mice, 3 sessions). **E**, Cross correlation of
1186 MPP bulk signal and summed GC signal during resting. Shaded grey area indicates standard
1187 error. **F**, Average MPP activity (red) and probability of granule cell activity across all mice, 3
1188 baseline sessions each, both aligned to the time point of network events ($n=3$ mice, 2008
1189 network events, shaded red area depicts SEM). **G**, Amplitudes of deconvolved events in

1190 MPP bulk data during locomotion (light red) und resting (dark red). **H**, Frequencies of all
1191 deconvolved MPP bulk events during locomotion and immobility (repeated measures
1192 ANOVA, $F_{(1,2)} = 255$, $p = 3 \times 10^{-6}$, $n = 3$ mice, 3 sessions). **I**, Frequencies of deconvolved
1193 events with amplitudes above two standard deviations (repeated measures ANOVA, $F_{(1,2)} =$
1194 27 , $p = 2 \times 10^{-3}$, $n = 3$ mice, 3 sessions). **J**, Delay of NEs to the closest identified MPP event.

1195 **Fig. 3: Pupil dynamics during network events.** **A**, Representative example of pupil size
1196 measurements during different locomotor states. Green dots indicate timepoints of network
1197 events. **B, C**, Average pupil diameters (grey lines) aligned to locomotion onsets (B) or offsets
1198 (C, blue lines) reveals pupil dilation at locomotion onsets, and constriction during locomotion
1199 offset. Shaded areas indicate standard error. GC activity stays on baseline value during
1200 change of behavioral state (green). **D**, Average pupil diameters during locomotion, during
1201 resting periods, and during network events. Asterisks indicate significant Bonferroni post-test
1202 at 5% level. **E**, Average rate of pupil diameter change during locomotion, during resting
1203 periods and during network events. Asterisks indicate significant Bonferroni post-test at 5%
1204 level. **F**, Averaging pupil diameters aligned to NE times (green bars) reveals pupil
1205 constriction during NEs. Shaded areas indicate standard error. ($n=6$ mice, 3 sessions). ($n=6$
1206 mice, 3 sessions).

1207 **Fig. 4: Network events are orthogonal, but repetitively recruit GC sub-ensembles.** **A**,
1208 Similarity between network events. Similarity of population vectors computed for individual
1209 network events. Comparisons were carried out between all possible pairwise combinations of
1210 vectors and quantified using cosine similarity. Inset: Mean number of orthogonal NEs for
1211 baseline sessions (Black bar) compared to shuffled data (gray bar) with SEM. Grey lines
1212 depict individual sessions. **B**, Graphical representation of the correlation matrix using
1213 Pearson's r for all cell combinations, with values for r being color coded. Data from one
1214 representative session in an individual mouse. **C**, Identification of clusters of correlated cells
1215 using agglomerative hierarchical clustering. Clusters were combined using a standardized
1216 Euclidean distance metric and a weighted average linkage method, until the mean of the
1217 cluster internal r -value reached a significance threshold. The 5% significance threshold was
1218 defined by creating a null-distribution of r values from randomized data sets, and is indicated
1219 for this particular experiment with a vertical line. Right panel in C depicts the reordered
1220 correlation matrix showing clusters of highly correlated cells. Only clusters whose mean intra-
1221 correlation exceeded the threshold were included in further analysis (significant clusters
1222 indicated with grey frames) **D**, Raster plot showing the reactivation of clusters identified in
1223 panel C during multiple episodes of running and immobility. Individual dots indicate
1224 participation of individual cells. Clusters are color-coded according to the agglomerative tree.
1225 Network events are indicated by vertical dashed lines. Running episodes are indicated at the
1226 lower border with the running speed (blue).

1227 **Fig. 5: Characterization of dentate gyrus place and speed neurons.** **A, B**, Place cells in
1228 the dentate gyrus. **A**, Representative polar plots of two significantly place-coding granule
1229 cells (left, middle), and one without significant place preference (right). Place coding is
1230 depicted as spiral plot, where each 360° turn of the spiral represents a transition through the
1231 1.5 m linear track without additional cues (baseline condition). Detected events are shown as
1232 black dots. The red line represents the place vector. The corresponding heatmap of
1233 normalized fluorescence is shown in the inset. In lower panels, the distributions for place
1234 vector lengths generated from shuffled data (see Methods) are shown (grey histograms), the
1235 place vector for the individual cell is indicated by the red line. **B**, Place field heatmaps of cells
1236 showing significant place preference. **C**, Representative examples of three significantly
1237 speed-modulated neurons (black traces, running speed depicted in cyan). **D**, Speed-

1238 modulated mean fluorescence signal of a representative example cell. Grey area indicates
1239 standard error. **E**, Mean fluorescence signals of all significantly speed-modulated cells.
1240 Normalized fluorescence is color coded and running speed is normalized to every individual
1241 mouse maximum running speed. **F**, Fractions of place and speed coding cells (cyan and
1242 green bar, respectively) normalized to all active cells (left panel) and only running active cells
1243 (right panel). Only a very small number of cells carried encoded both features (dark green
1244 bar).

1245 **Fig. 6: Increasing sensory cues is associated with enlargement of network events and**
1246 **increased incorporation of place cells.** **A**, Network events comprise more granule cells in
1247 cue-enriched environments. Cumulative probability of network event size (number of cells
1248 per network event) for baseline and cue enriched condition (dark and light grey lines,
1249 respectively). **B**, Cumulative probability of participation in multiple network events per cell for
1250 baseline and cue enriched condition (dark and light grey lines, respectively). **C**, Fraction of
1251 place and speed cells that participate in network events (total number of place/speed cells
1252 equals 100%). **D**, Relation of place and speed cells to correlated cell clusters (c.f. Fig. 4).
1253 Fraction of the total number of clusters containing place cells (cyan), speed cells (light
1254 green), or both (dark green). Gray indicates clusters containing neither place nor speed cells.
1255 **E**, Mean number of place and speed cells per cluster, in baseline and cue enriched
1256 conditions, $n = 9$ mice. **Fig. 7: Similarity of activity patterns during network events to**
1257 **population patterns during locomotion.** **A**, Color code for position on the linear track used
1258 in panels B. **B**, Trajectories during an individual representative session plotted in a three-
1259 dimensional coordinate system corresponding to the first three PCA components (Comp 1-
1260 3). **C**, Trajectories calculated from CA1 Ca^{2+} -imaging data during an individual
1261 representative session for comparison. **D**, average peak value of weight-autocorrelations at
1262 $\Delta\text{lap} = 1$ (ANOVA, $F_{(1,3)} = 88.32$, $p = 2 \times 10^{-30}$, * Bonferroni post-test at $p < 0.05$, *** Bonferroni
1263 post-test at $p < 0.001$). **E**, Schematic of the procedure for comparing population activity during
1264 network events (NE) and locomotion. Population activity is represented by 3 cells (upper
1265 traces), recorded during running and quiet immobility (blue trace indicates speed). Time point
1266 of three network events is indicated schematically by red lines. Activity during network events
1267 (NE) was used to perform PCA, computing the transformation matrix V_{net} . Similarly, PCA was
1268 performed on the neuronal population activity only from running periods (speed indicated in
1269 blue, bordered by vertical grey dashed lines), to generate the transformation matrix V_{run}
1270 representing the covarying activity during locomotion. **F**, Schematic description of the
1271 procedure for projecting co-variances of running activity into the PCA basis of network events
1272 (or shuffled data). Grey dots show covarying activity of two representative cells during
1273 running. The blue graph denotes the projection into the locomotion PCA-space using V_{run}
1274 and the width of the distribution shows the projected variance. The red graph shows the
1275 same information for the network space using V_{net} . **G**, Individual example of shuffle analysis
1276 for a representative session. The vertical red line indicates the observed projected variance
1277 explained normalized to variance explained in the original space (50 % of the overall
1278 variance). The observed variance explained is larger than the shuffled distribution (blue
1279 bars), indicating that the population activity during locomotion and network events is more
1280 similar than expected by chance (i.e. for network activity without correlations). **H**, Cartoon
1281 illustrating NE structure for four cells and three synchronous events. **I**, Upper panel: Cartoon
1282 illustrating the first shuffling procedure where each cells time series is shifted by a
1283 randomized time interval. Lower panel: Fraction of sessions in which comparisons of
1284 population activity were significant vs. chance level for the two cue conditions and all
1285 similarity measures ($n = 8$ mice, 1 session per condition, see Fig. 7-figure supplement 3 for
1286 comparisons to shuffled datasets for all sessions). **J**, Upper panel: Cartoon illustrating the

1287 second shuffling procedure where cell IDs within each NE are randomly shuffled. This
1288 approach randomizes NE-composition while maintaining the number of cells per NE. Lower
1289 panel: Analogous to I. **K**, Upper panel: Cartoon illustrating the third shuffling procedure
1290 where the NE participation is randomly shuffled for each cell. This approach randomizes NE-
1291 participation while maintaining the activity level for each cell. Lower panel: Analogous to I.

1292 **Fig. 8: Inhibition of dentate granule cell activity during immobility prevents memory**
1293 **acquisition.** **A**, Schematic of the bilateral optogenetic inhibition of the dentate gyrus granule
1294 cells expressing eNpHR. **B**, Schematic of the experimental procedure. In the acquisition
1295 phase, mice were familiarized with an arena containing two objects. Following an
1296 intermediate period of 90 minutes, the mice were placed in the same arena in which one
1297 object was moved slightly. **C**, **D**, Representative sessions from acquisition trials in control
1298 (eYFP) mice and mice expressing eNpHR in granule cells showing the tracking of the mouse
1299 center of mass (dashed white lines), as well as normalized occupancy within the arena. **E**,
1300 Discrimination index from the acquisition trial quantifying the specific exploration activity of
1301 the objects relative to one another (see Methods), with 0 values indicating equal exploration
1302 (see Methods). **F**, Total time spent exploring the objects in the eYFP and eNpHR groups
1303 during the acquisition trial. **G**, **H**, Representative sessions from recall trials depicted as
1304 shown in B, C. **I**, Discrimination index for recall trials, showing strong preference for the
1305 displaced object in the eYFP group, but not the eNpHR group if granule cell activity was
1306 inhibited during acquisition trials only during immobility. **J**, Total time spent exploring the
1307 objects in the eYFP and eNpHR groups during the recall trial (n=6 animals for eNpHR group,
1308 n=9 animals for eYFP group).

1309

1310 **Figures supplement captions:**

1311 **Figure 1-figure supplement 1: Dual color two-photon imaging in the dentate gyrus.** **A**,
1312 Representative hippocampal sections from three different mice with expression of jRGECO
1313 in the MPP (red), GCaMP6s in granule cells (green), and DAPI as nuclear staining. **B**, Setup
1314 of the 2-photon microscope for dual-color two-photon imaging. To allow efficient excitation of
1315 both genetically encoded Ca^{2+} indicators, we established excitation with two pulsed laser
1316 sources at 940 and 1070 nm. **C**, **D**, Dimensions of flat, custom head fixation ring. **F**, conical
1317 transparent inset used to maximize NA in deep imaging. Linked to Methods. **D**, Properties of
1318 the linear track designs for baseline, cue-enriched and zone configuration. **H**, **I**, **J**,
1319 Locomotion on the linear track. Neither the total distance run on the linear track (D), nor the
1320 average running speed (E), nor the fraction of time spent running differed significantly
1321 between the baseline and cue-enriched and zone conditions (n.s., ANOVA, $p = 0.31, 0.58$
1322 and 0.67 respectively).

1323 **Figure 1-figure supplement 2: Granule cell activity during locomotion on empty**
1324 **textured belt.** **A**, Image plane for granule cell recording in the dentate gyrus. **B**, One
1325 representative component of non-negative matrix factorization. Upper panel: spatial
1326 component as extracted from image stack. Middle panel: Corresponding $\Delta\text{F}/\text{F}$ trace
1327 generated from a ROI drawn around the corresponding somatic region. Lower panel:
1328 Extracted $\Delta\text{F}/\text{F}$ trace (gray) with deconvolved trace (black). Identified event onsets are
1329 depicted with vertical green lines. **C**, **D**, Frequencies of Ca^{2+} events (C) and magnitude of
1330 Ca^{2+} transients during each recording session (D) recorded during quiet immobility (rest, dark
1331 bars) and locomotion (run, light bars) on an empty textured belt (data from 3 sessions per
1332 animal, n=9 mice, comparisons between running and resting states ANOVA, n.s.). **E**,
1333 Distribution of event frequencies for all cells. Black bars represent events during resting

1334 periods, grey bars represent frequencies during locomotion (data from 3 sessions per animal,
1335 n=9 mice).

1336 **Figure 1-figure supplement 3: Shuffling analyses demonstrating that network events**
1337 **do not arise by chance. A,** Average number of identified network events plotted against
1338 different used thresholds for the size of network events in terms of numbers of synchronously
1339 active cells (green line, shaded area depicts SEM, n = 3 mice, 3 sessions). Shuffled data
1340 null-distribution is created by randomly shuffling event times for every individual cell (grey
1341 line, shaded area depicts SEM). **B,** Same as A, but using a shuffling approach where traces
1342 are randomly shifted with respect to each other (red line, shaded area depicts SEM). **C,**
1343 Same as A and B, but using a shuffling method where event times are randomly shuffled for
1344 locomotion and immobility periods separately (Purple line, shaded area depicts SEM). **D-I,**
1345 Six representative example data sets. Left panels: Raster plot of event onsets (grey dots)
1346 and identified network events (Colored dots) during episodes of locomotion and immobility
1347 (blue line). Right panels: Number of network events identified for different threshold (green
1348 lines). All three different shuffling approaches are shown in each panel (grey, red, purple
1349 lines for the shuffling approaches depicted in panels A-C, respectively). Error bars depict
1350 standard deviation. All shuffling approaches yield uniform results.

1351 **Figure 4-figure supplement 1: Clustering of cells active during network events into**
1352 **correlated sub-ensembles via a correlation matrix. A_H,** Examples of correlation
1353 matrices after hierarchical clustering from four of the nine mice investigated. Those clusters
1354 with an intra-cluster correlation above threshold that were considered for further analysis are
1355 indicated with a grey frame. Upper row (A-D) shows baseline condition and lower row (E-H)
1356 cue-enriched condition.

1357 **Figure 5-figure supplement 1: Activity of granule cells and MPP inputs in cue-enriched**
1358 **conditions. A,** Average frequencies of Ca^{2+} events (A) for baseline and cue-enriched
1359 conditions recorded during quiet immobility (rest, dark bars) and running (run, light bars).
1360 Data from n=9 mice, last baseline session and cue-enriched session for panels A and B (2-
1361 way ANOVA, run vs. rest: $F_{(1,32)} = 1.71$, $p = 0.20$, baseline vs cue-enriched $F_{(1,32)} = 1.80$, $p =$
1362 0.19). **B,** Same as A for the magnitude of Ca^{2+} transients (2-way ANOVA, run vs. rest: $F_{(1,32)}$
1363 $= 1.67$, $p = 0.21$, baseline vs cue-enriched $F_{(1,32)} < 0.01$, $p = 0.99$) **C,** Distribution of event
1364 frequencies for all cells for the cue-enriched condition. **D,** Under cue-enriched conditions,
1365 network events also occurred mainly during immobility. Mean number of network events per
1366 recording session during running (light green) and resting (dark green). Grey bars depict
1367 shuffled data for each condition. Section sign indicates ANOVA $F_{(3,28)} = 8.6$, $p = 0.0003$,
1368 asterisk indicates Bonferroni post-test resting vs. shuffled $p = 0.0019$). **E,** Cos-similarity
1369 between network events under cue-enriched conditions. Similarity of population vectors
1370 computed for individual network events. Comparisons were carried out between all possible
1371 pairwise combinations of vectors and quantified using cosine similarity. The number of
1372 orthogonal network events were significantly higher than expected by chance (Comparison
1373 shuffled vs. real data, Wilcoxon signed rank test $p = 0.031$). **F-J,** Activity of MPP inputs in the
1374 cue-enriched condition. Data from n = 4 mice, one mouse included additionally to Fig. 1F that
1375 had only jRGECO expression in MPP, but no granule cell signal for panels G-J. Shaded
1376 areas indicate standard errors. **F,** Mean fluorescence averaged during resting (dark red) and
1377 running (light red, n = 4) in cue-enriched trials. ANOVA for running vs. immobile states $F_{(1,3)} =$
1378 9.64 , $p = 0.02$. **G,** Variance of MPP bulk signal during resting (dark red) and running (light
1379 red, n = 4) in cue-enriched trials. ANOVA for running vs. Immobile states n.s. **H,** Cross
1380 correlation of MPP bulk signal and summed GC signal during resting. Grey shaded area

1381 indicates standard error. **I**, In cue-enriched conditions, MPP activity also increases at
1382 transitions from immobility to running (red line, MPP activity, blue line indicates running
1383 speed, $n = 4$). **J**, Average MPP activity (red) and probability of granule cells being active in
1384 cue-enriched trials, both aligned to the time point of network events. Red shaded areas
1385 indicate standard error.

1386 **Figure 7-figure supplement 1: Analysis of population activity in dentate gyrus and the**
1387 **CA1 subfield of the hippocampus using PCA, ICA and GPFA. A-C**, Upper panels depict
1388 the first three components from representative sessions (A: PCA, B: ICA, C: GPFA) plotted in
1389 a coordinate system. The color code refers to the place on the linear track, with the same
1390 locations represented in the same color. **D-F**, As in A-C, but for CA1 neurons. Note the
1391 smooth and repetitive trajectories. Linked to Fig. 7.

1392 **Figure 7-figure supplement 2: PCA-based analysis of spatial representation in DG and**
1393 **CA1. A-D**, Trajectories of first three components for DG example recordings in different
1394 environments (A-C for baseline, cue-enriched and zones, respectively) and CA1 data (D).
1395 The animals' position is color coded analogous to Fig. 7-figure supplement 1. **E-H**, Weights of
1396 five first principal components plotted against the animal position during the first 6 laps of the
1397 recording. **I-L**, normalized autocorrelation of five first PCA-weights from example data
1398 calculated with respect to different laps. Place information in weights leads to peaks at
1399 integer multiples of Δ lap. **M-P**, autocorrelations from five first components averaged for all
1400 animals ($n = 9$ animals for baseline and cue-enriched, $n = 3$ animals for DG zones, $n = 5$
1401 animals for CA1).

1402 **Figure 7-figure supplement 3: Similarity of individual network events to population**
1403 **activity during running.** Data from all sessions under baseline and cue-enriched conditions
1404 are depicted (as indicated on the leftmost border of the figure) for all three measures. PCA
1405 similarity using the vector projection method introduced in this paper (see Methods), cosine
1406 similarity measures (*Krzanowski, 1979*) and EROS (*Yang, K., Shahabi, C., 2004*) are
1407 depicted in the leftmost, middle and rightmost columns, respectively. In all graphs, shuffled
1408 data distributions generated with shuffle method 1 are shown in light blue, a vertical red line
1409 indicates the observed similarity value between network and locomotion related population
1410 activity in the particular session. P-values are indicated above each graph. In the variance
1411 projection method, values were normalized to the locomotion related variances projected into
1412 the locomotor states. As expected, this results in a high proportion of explained variance.
1413 Linked to Fig. 7.

1414 **Figure 8-figure supplement 1: Establishing a dentate gyrus-dependent variant of the**
1415 **object pattern separation task. A**, Schematic of the bilateral optogenetic inhibition of the
1416 dentate gyrus granule cells expressing eNpHR. **B**, Description of the task. Following
1417 familiarization with the object location, one of the objects is moved in a subsequent recall
1418 session, and the extent to which mice explore the moved vs. stationary object is examined.
1419 These trials can be repeated allowing to explore the effects of variable movement of the
1420 objects. **C**, Schematic of possible object locations for the displaced object. Displacement was
1421 randomized for each animal, such that either the left or the right object was displaced, in
1422 either a forward or back direction (LB i.e. corresponding to left, back, and RF to right,
1423 forward). The experiment used four possible new locations along a vertical axis, increasing
1424 from minor displacement (3 cm) to maximal displacement, indicated by numbers 1-4. **D**,
1425 Stitched wide-field image of a hippocampal slice showing expression of NpHR-eYFP in both
1426 DGs. **E**, Results of light-based inhibition of granule cells during acquisition and recall trials for

1427 different degrees of object separation indicate on the x-axis (eNpHR group, n=4, green bars)
1428 vs. an eYFP expressing control group (n=3, black bars). The effect of granule cell inhibition is
1429 most pronounced for intermediate degrees of object movement. **F**, Representative, typical
1430 discharge behavior of a granule cell. **G**, inhibition of granule cell firing evoked with long
1431 current injections by light-based activation of NpHR (green vertical bars) with continuous
1432 stimulation. **H**, quantification of firing rates before, during and after illumination for continuous
1433 stimulation (ANOVA, $F_{(2,5)} = 28.30$, $p = 0.001$, Dunnett's multiple comparison test, asterisks
1434 indicate 5% significance level). **I**, like F with pulsed stimulation at 50% duty cycle and 20 Hz
1435 (d). **J**, like G with pulsed stimulation (ANOVA, $F_{(2,5)} = 61.00$, $p = 0.001$, Dunnett's multiple
1436 comparison test, asterisks indicate 5% significance level). **K, L**, Estimation of light-induced
1437 warming within brain tissue for continuous illumination (K) or pulsed illumination at 50% duty
1438 cycle and 20 Hz (L) at intensities used for the behavioral experiments. Predicted temperature
1439 changes are plotted as a function of time and depth. **M**, Analysis of warming over time,
1440 showing that the warming effects of pulsed light stimulation are asymptotic, and remain
1441 below 0.4 °C at a distance of 300 μm from the fiber front end. Linked to Fig. 8.

1442 **Figure 8-figure supplement 2: Inhibition of dentate granule cell activity during**
1443 **locomotion only in the acquisition trial impairs memory formation in the OPS task. A,**
1444 Description of the experimental protocol. In the acquisition phase, mice were familiarized with
1445 an arena containing two objects. Following an intermediate period of 90 minutes, the mice
1446 were placed in the same arena in which one object was moved slightly. Inhibition of granule
1447 cells was carried out not at all, during periods of quiet immobility, or during periods of
1448 locomotion in the acquisition trial in three consecutive experiments. **B**, Discrimination indices
1449 for animals performing the OPS task during acquisition. Experiments were performed in three
1450 conditions. First, granule cells were not inhibited. In a second run GC activity was
1451 optogenetically inhibited during resting periods. In the third run GC activity was inhibited
1452 exclusively during running periods (Repeated measures ANOVA, $F_{(1,14)} = 1.48$, $p = 0.28$, $n =$
1453 5). **C**, Animals showed comparable exploration times during the acquisition trial in all three
1454 conditions (Friedmann test, $p = 0.69$). **D**, During the recall trial animals were only able to
1455 discriminate the displaced object, when no GC inhibition had happened during the acquisition
1456 trial. No difference was found for the animals depending on whether inhibition had happened
1457 during immobility or locomotion (Repeated measures ANOVA, $F_{(1,14)} = 54.58$, $p = 0.0003$.
1458 Bonferroni post-tests: none vs. rest, $p = 0.0026$; none vs. run, $p = 0.0076$; rest vs. run $p =$
1459 0.14 , $n = 5$). **E**, Exploration times did not differ with regard to the experimental condition
1460 (Friedmann test, $p = 0.78$). **Figure 8-figure supplement 3: Inhibition of dentate granule**
1461 **cell activity during immobility in the acquisition trial only in non-object locations**
1462 **impairs memory formation in the OPS task. A**, Description of the experimental protocol.
1463 In the acquisition phase, mice were familiarized with an arena containing two objects.
1464 Following an intermediate period of 90 minutes, the mice were placed in the same arena in
1465 which one object was moved slightly. Inhibition of granule cells was carried out only during
1466 periods of quiet immobility in the acquisition trial, and only if the periods of immobility were
1467 not adjacent to the objects. **B, C**, Representative sessions from acquisition trials in control
1468 (eYFP) mice (b, $n=10$) and mice expressing eNpHR in granule cells (c, $n=4$) showing the
1469 tracking data (dashed white lines), as well as occupancy within the open field as a heat map.
1470 **D**, Discrimination index quantifying relative exploration times of the two objects, with 0 values
1471 indicating equal exploration (see Methods). Comparison between groups n.s., t-test with
1472 Welch correction $p=0.3537$. **E**, Total time spent exploring the objects in the eYFP and
1473 eNpHR groups during the acquisition trial. Comparison between groups n.s., t-test with
1474 Welch correction $p=0.6126$. **F, G**, Representative sessions from recall sessions. **H**,

1475 Discrimination index for recall trials, showing a significant reduction in the recognition of the
1476 displaced object in the eNpHR group. t-test with Welch correction $p=0.0018$. **I**, Total time
1477 spent exploring the objects in the eYFP and eNpHR groups during the recall trial.
1478 Comparison between groups n.s., t-test with Welch correction $p=0.4285$. **J**, Inhibition of
1479 dentate granule cell activity during immobility only during recall trials does not significantly
1480 impair performance in the OPS task. In the acquisition phase, mice were familiarized with an
1481 arena containing two objects. Following an intermediate period of 90 minutes, the mice were
1482 placed in the same arena in which one object was moved slightly. Inhibition of granule cells
1483 was carried out only during periods of quiet immobility in the recall trial. **K, L**, Representative
1484 sessions from acquisition trials in control (eYFP) mice (b, $n=11$) and mice expressing eNpHR
1485 in granule cells (c, $n=6$) showing the tracking data (dashed white lines), as well as occupancy
1486 within the open field as a heat map. **M**, Discrimination index quantifying relative exploration
1487 times of the two objects, with 0 values indicating equal exploration (see Methods).
1488 Comparison between groups n.s., t-test with Welch correction $p = 0.8613$. **N**, Total time
1489 spent exploring the objects in the eYFP and eNpHR groups during the acquisition trial.
1490 Comparison between groups n.s., t-test with Welch correction $p = 0.6097$. **O, P**,
1491 Representative sessions from recall sessions. **Q**, Discrimination index for recall trials,
1492 showing no significant reduction in the recognition of the displaced object in the eNpHR
1493 group. Comparison between groups n.s., t-test with Welch correction $p = 0.2802$. **R**, Total
1494 time spent exploring the objects in the eYFP and eNpHR groups during the recall trial.
1495 Comparison between groups n.s., t-test with Welch correction $p = 0.8236$.

1496

1497 **Supplementary file captions:**

1498 **Supplementary File 1:** Spread Sheet containing statistical test results for present data with
1499 respective figure numbers.

1500

1501 **Supplementary video captions:**

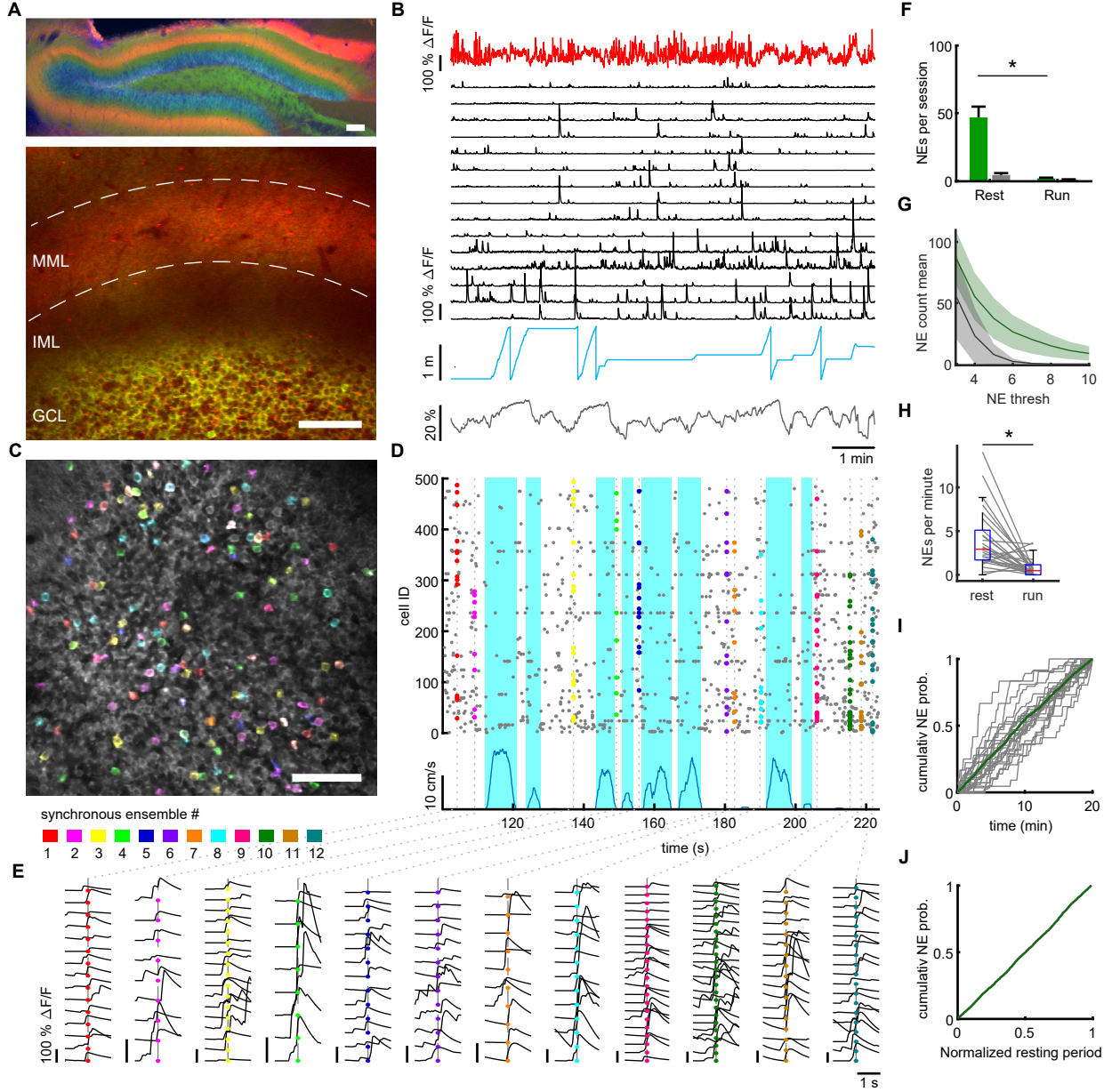
1502 **Video 1:** Video showing activity of granule cells and MPP, corresponding to Fig. 1A, B.

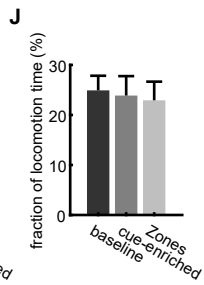
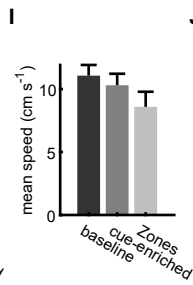
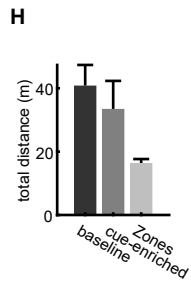
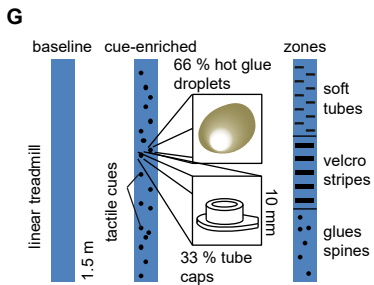
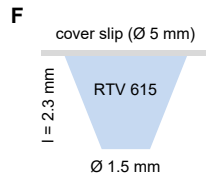
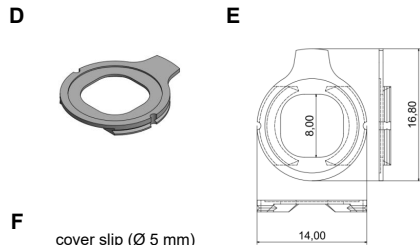
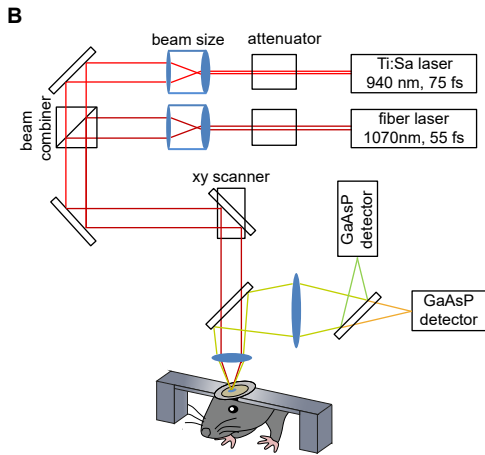
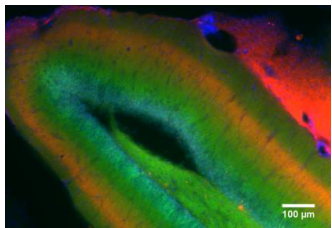
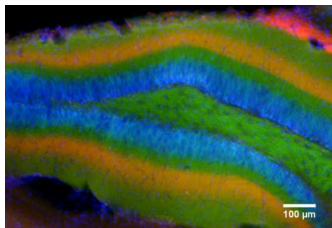
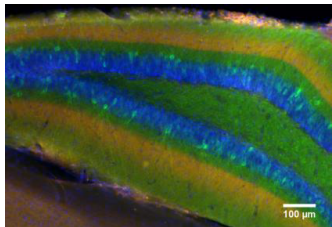
1503 **Video 2:** Video showing network events, corresponding to Fig. 1C

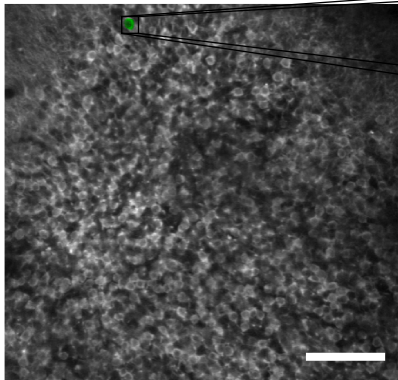
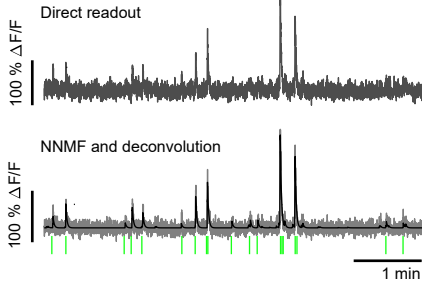
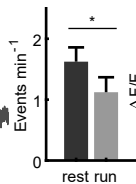
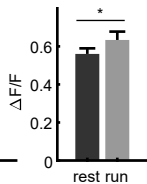
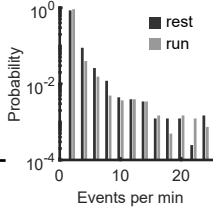
1504

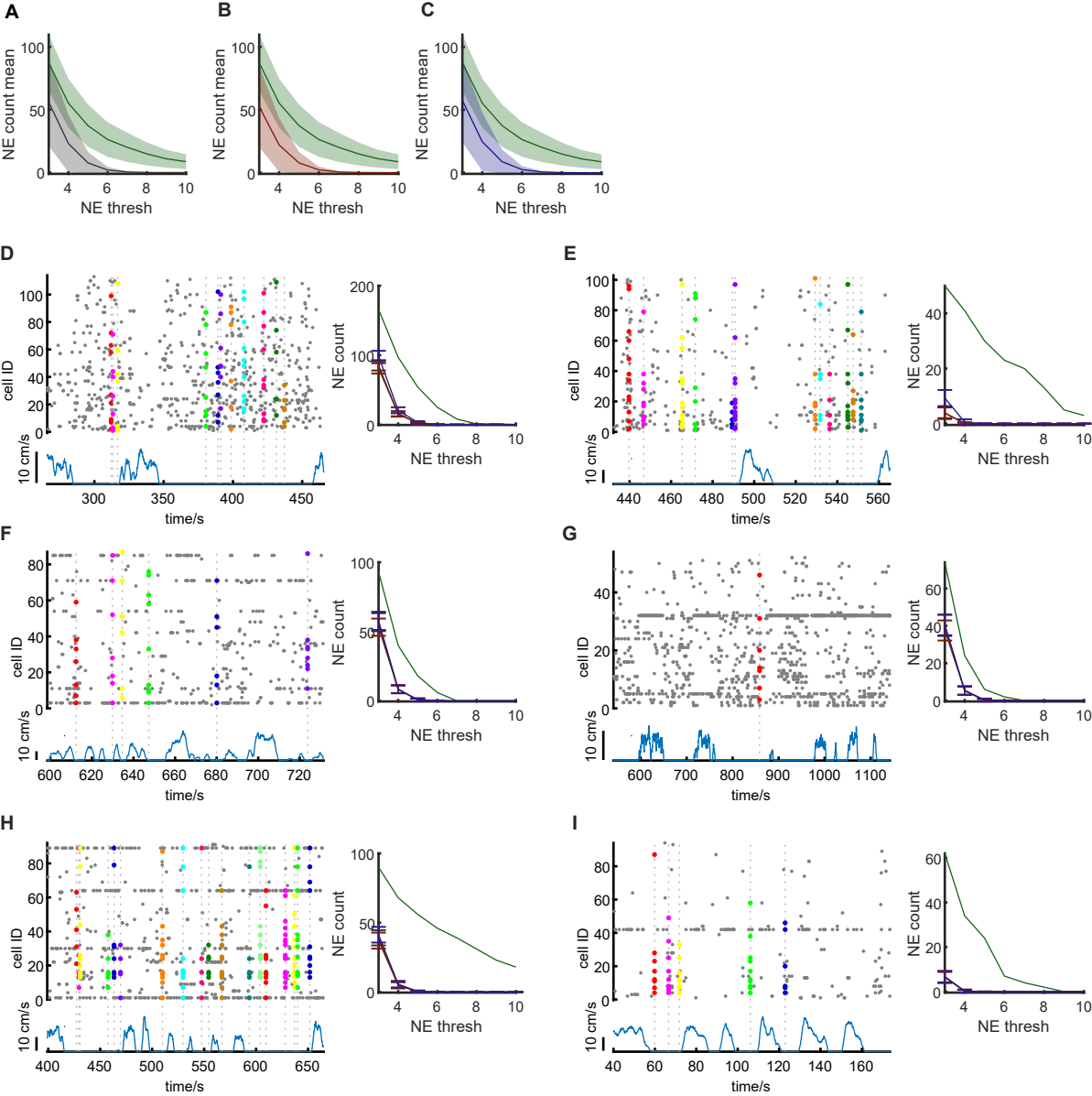
1505 **Supplementary References**

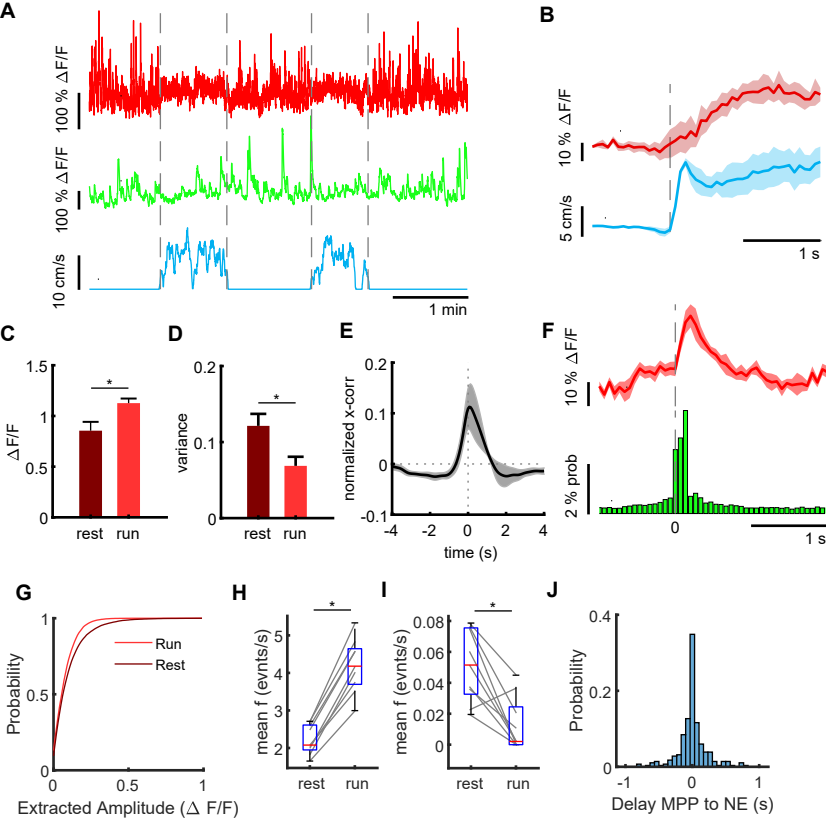
- 1506 1. Krzanowski, W.J. Between-Groups Comparison of Principal Components. *Journal of the American*
1507 *Statistical Association* **74**, 703–707 (1979).
1508 2. Yang, K., Shahabi, C. A PCA-based similarity measure for multivariate time series. *Proceedings of*
1509 *The 2nd ACM International Workshop on Multimedia Databases (MMDB)*, 65–74 (2004).

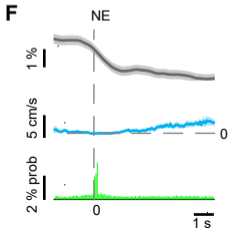
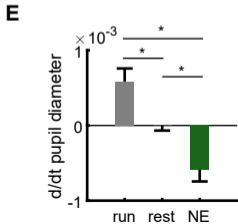
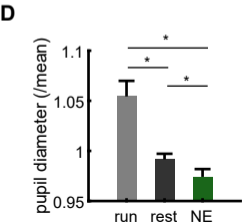
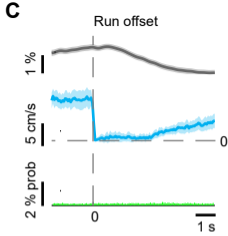
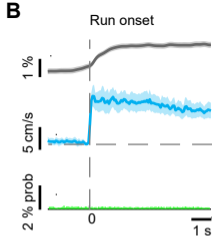
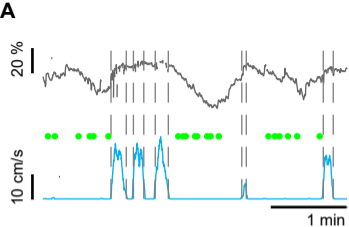


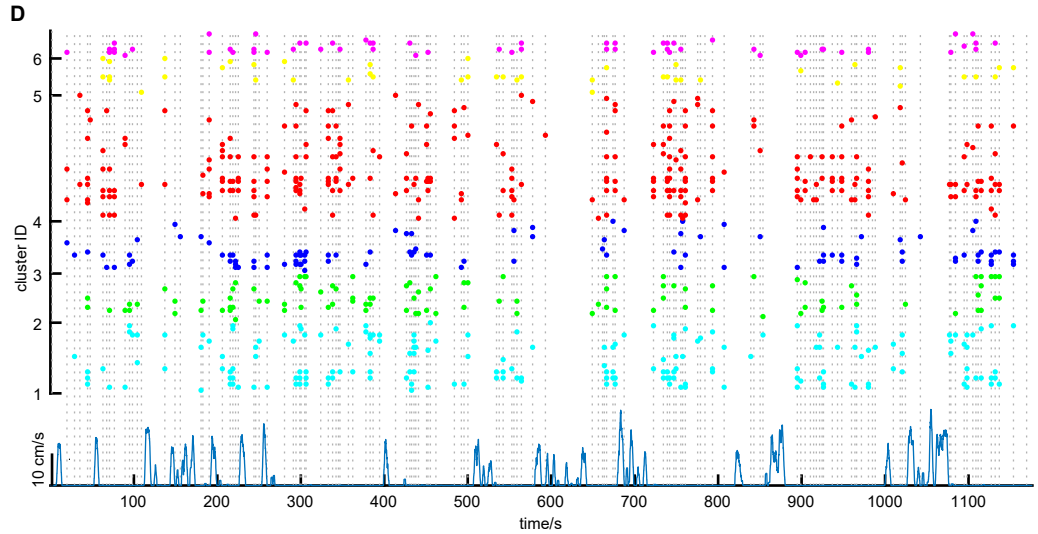
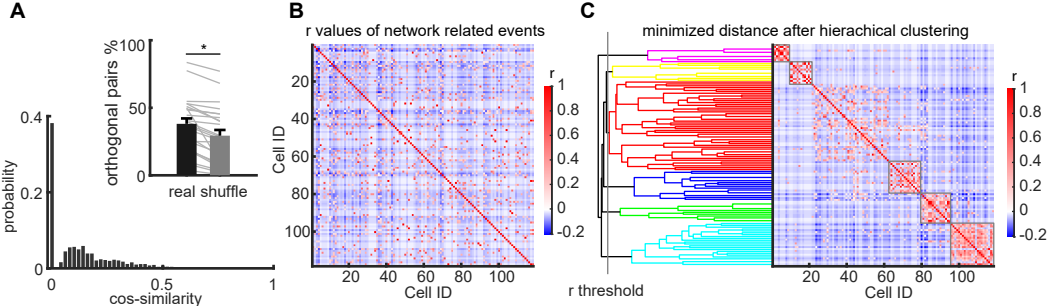


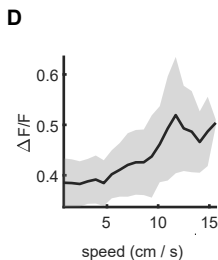
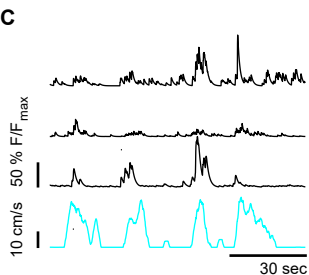
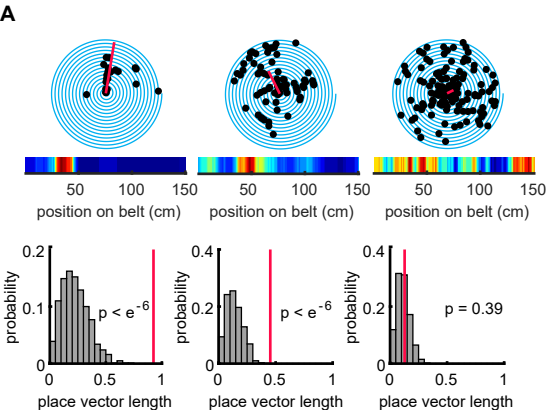
A**B****C****D****E**







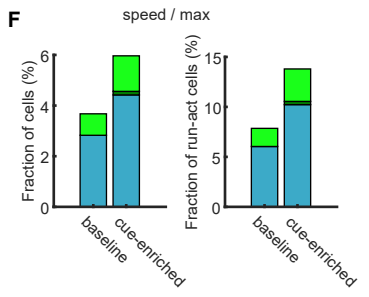
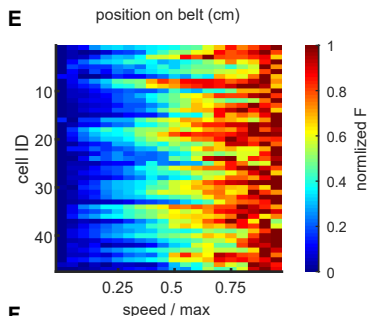
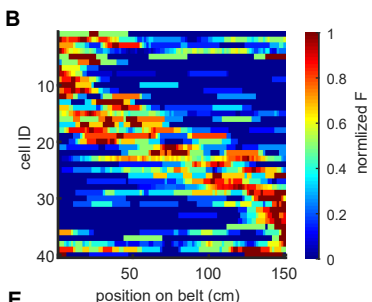


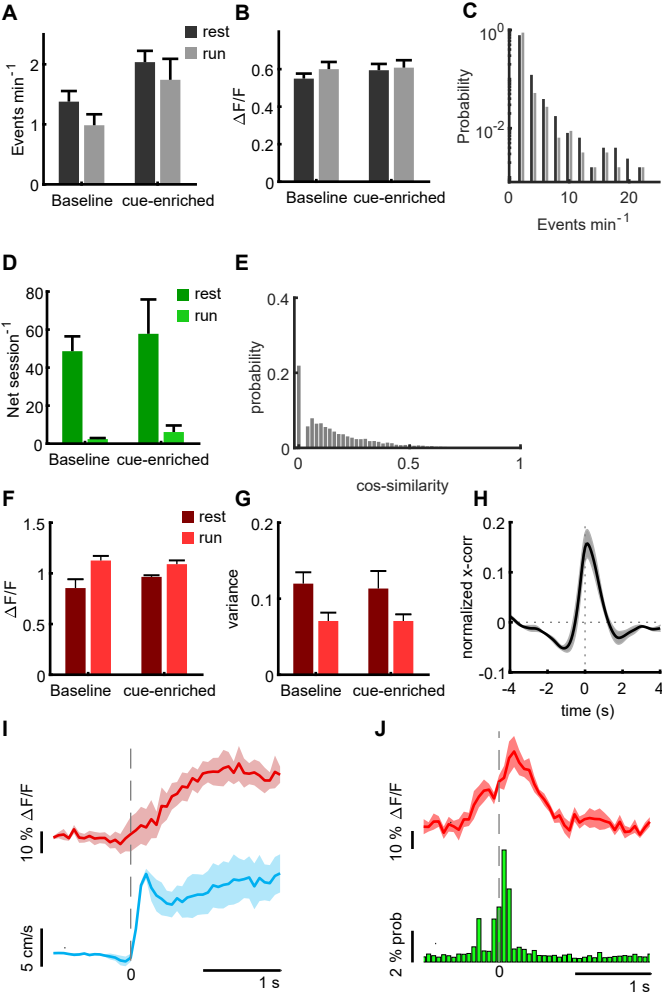


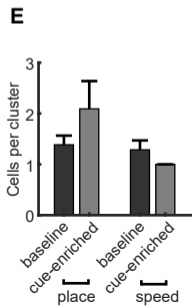
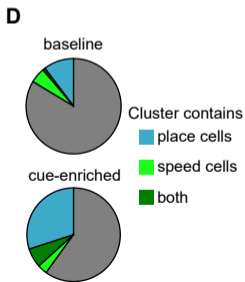
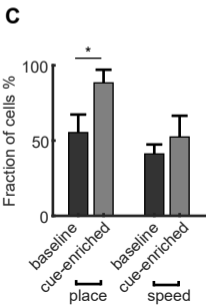
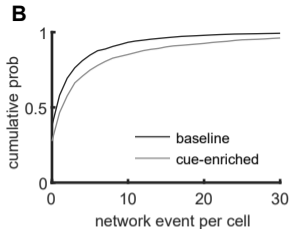
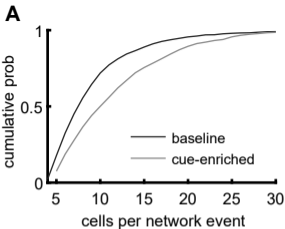
speed cells ■

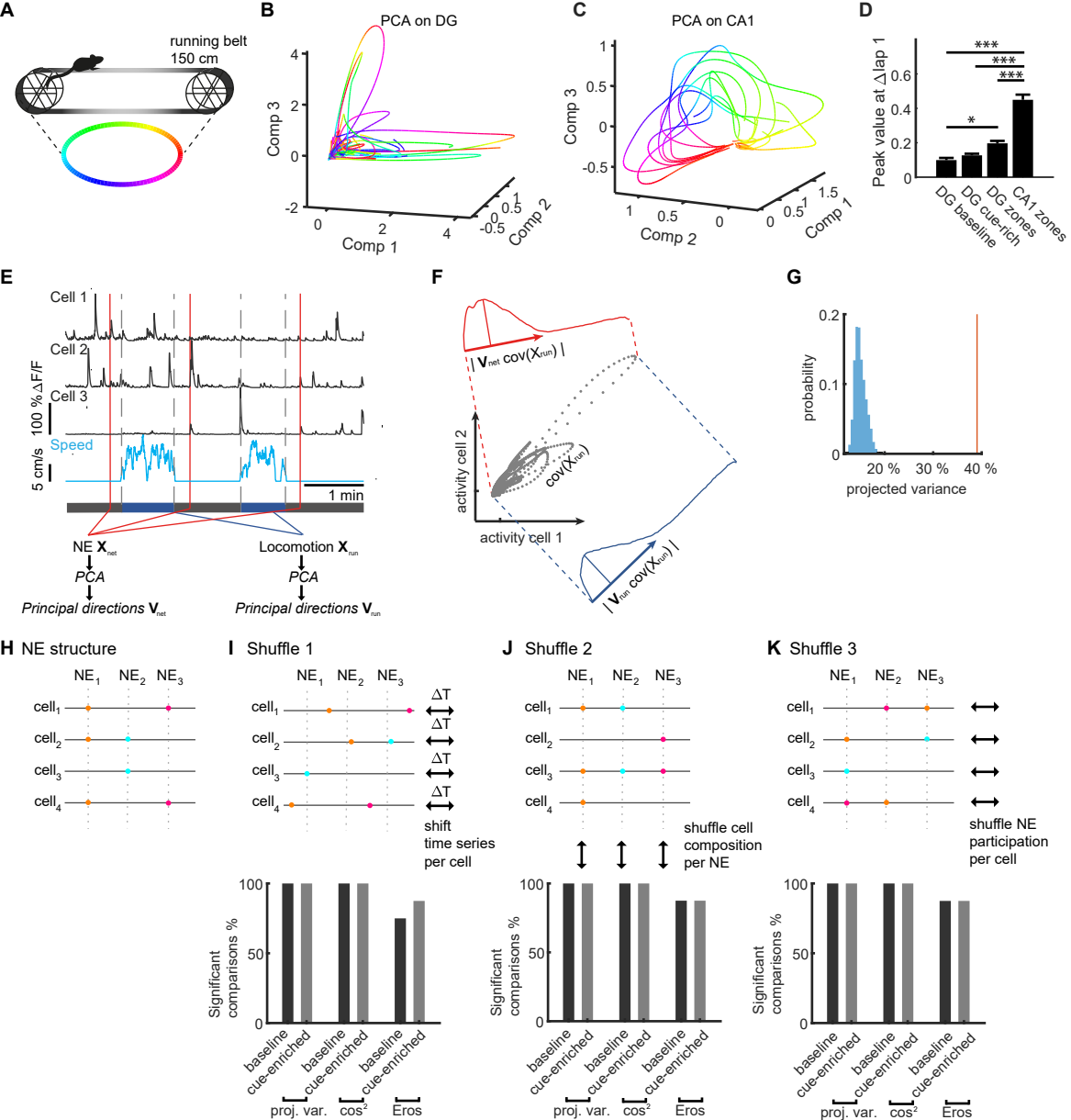
both ■

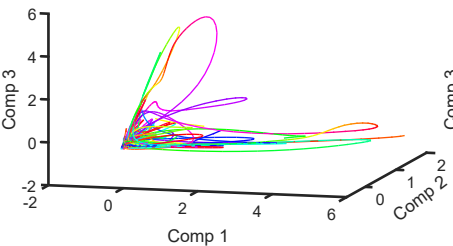
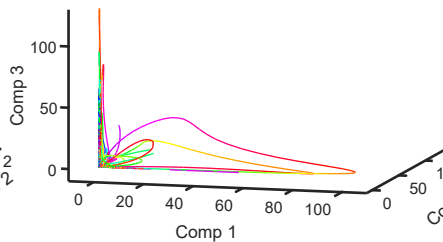
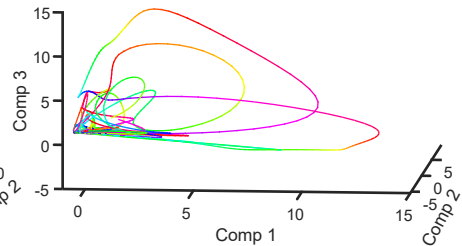
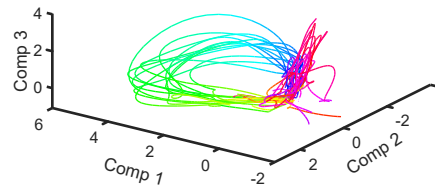
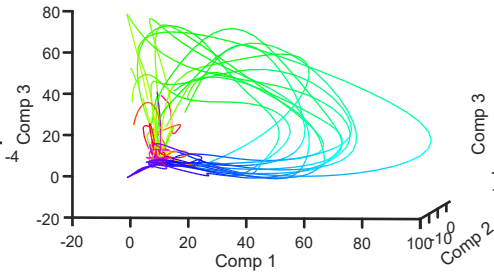
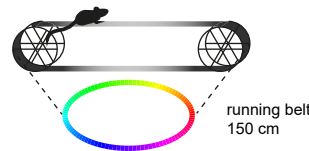
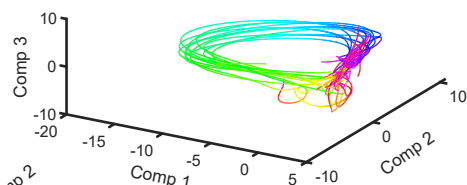
place cells ■

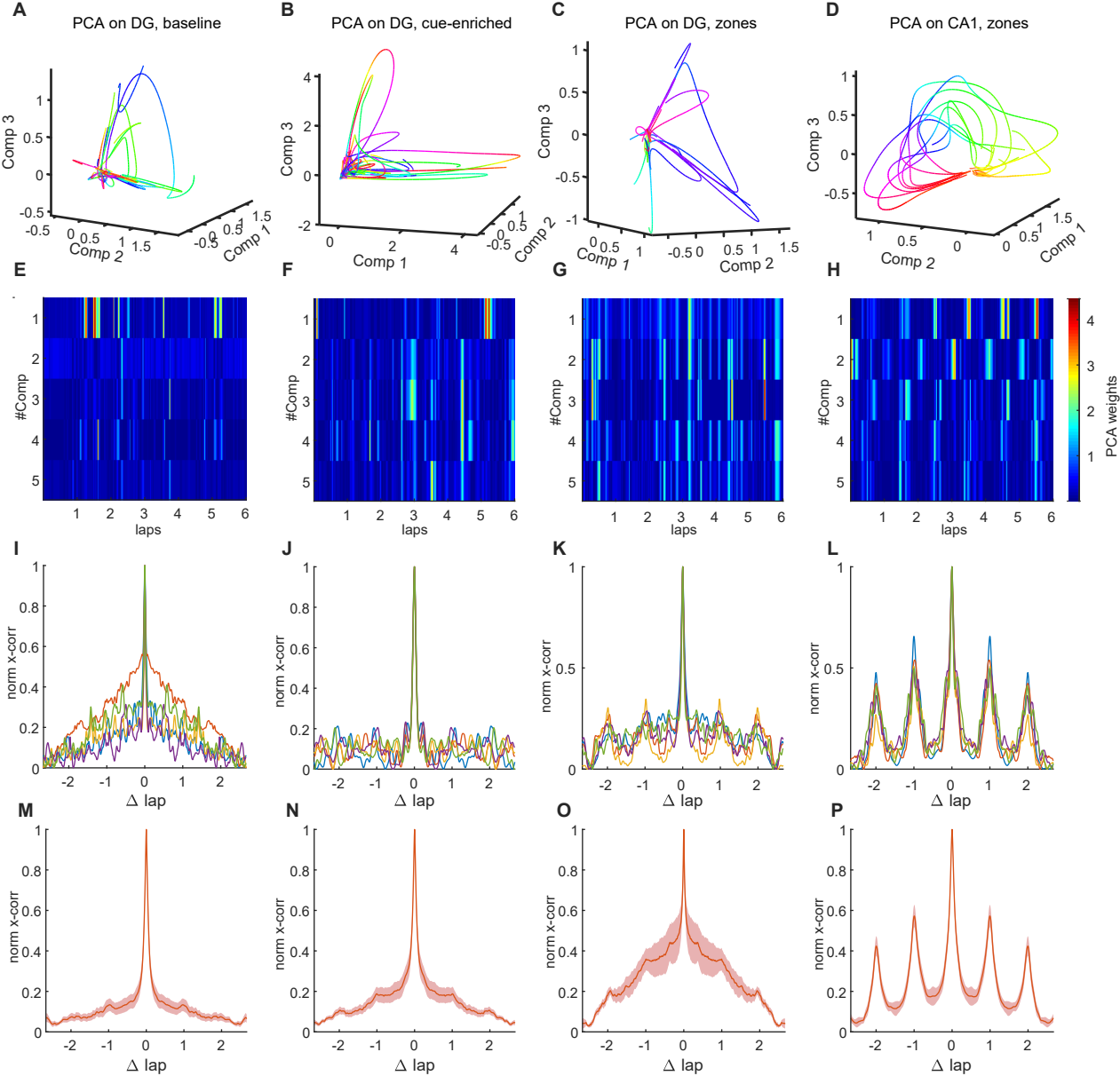


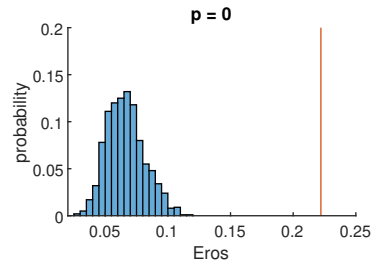
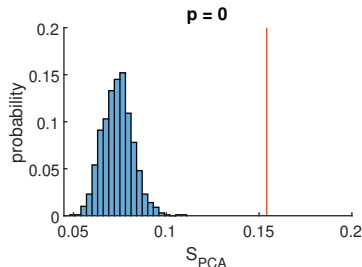
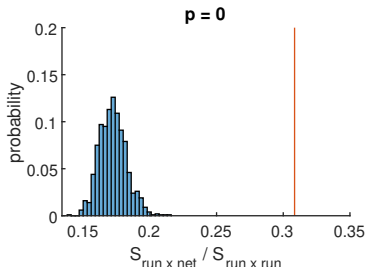
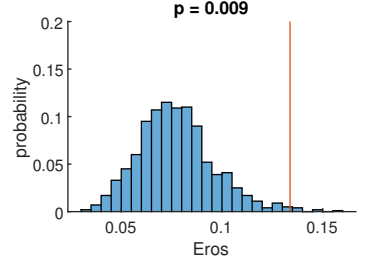
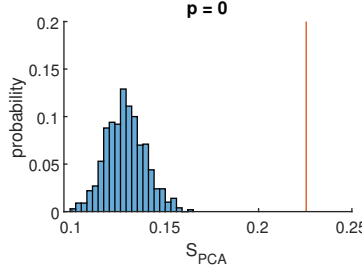
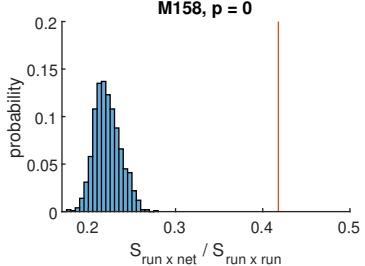
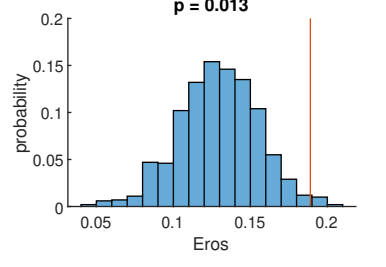
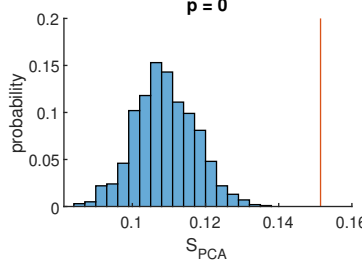
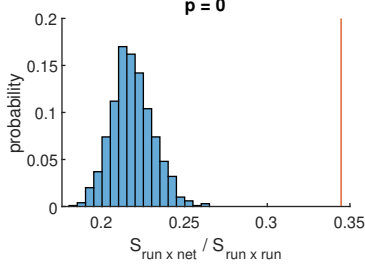
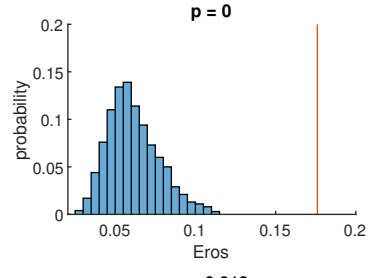
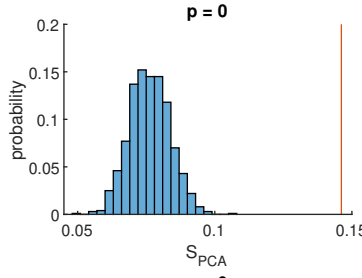
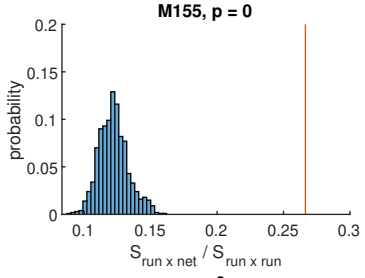
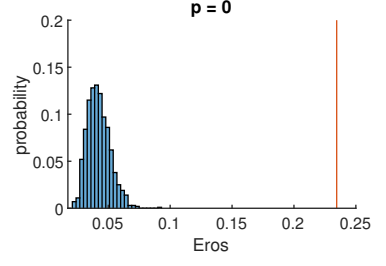
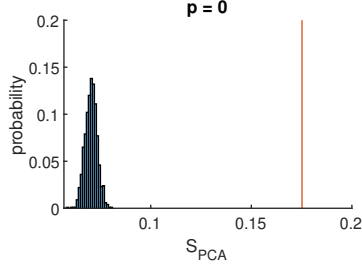
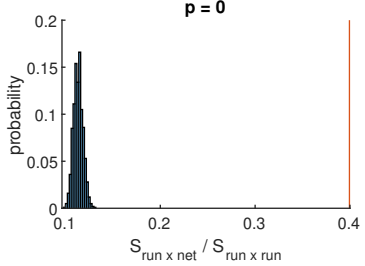
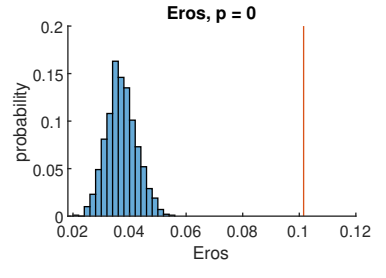
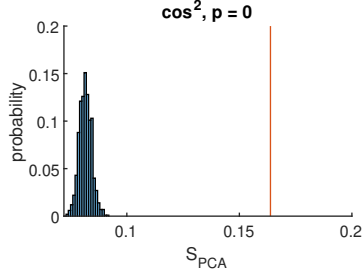
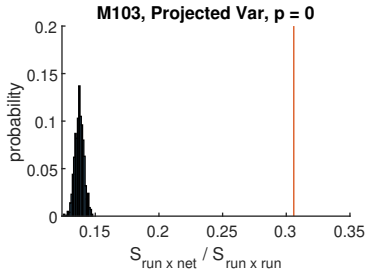


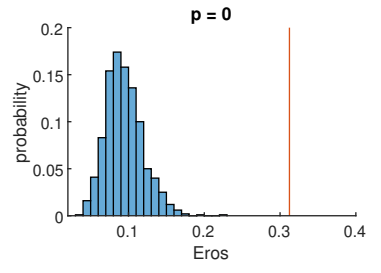
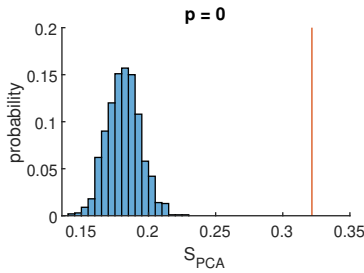
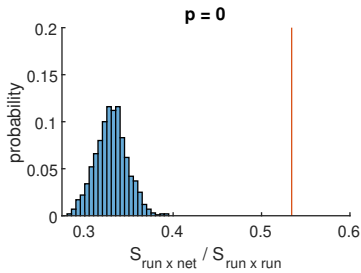
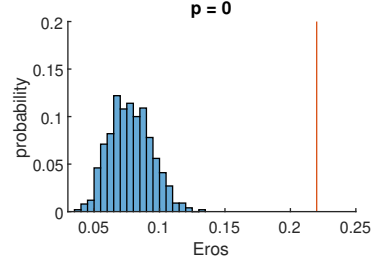
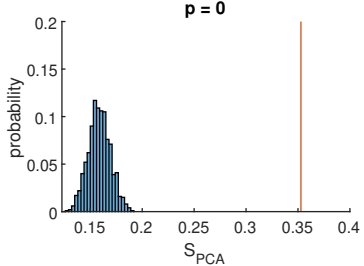
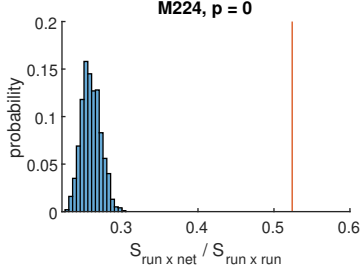
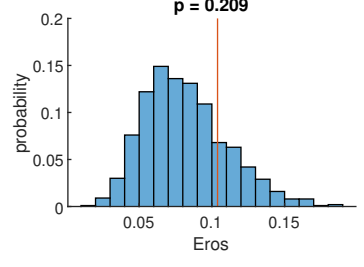
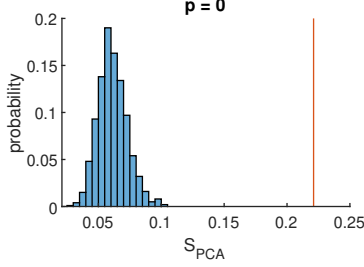
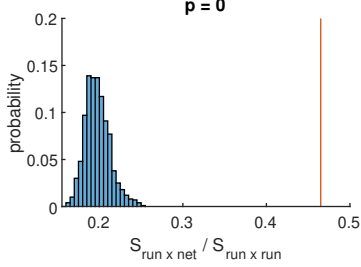
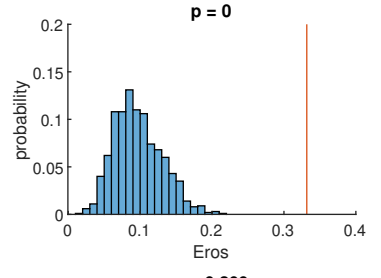
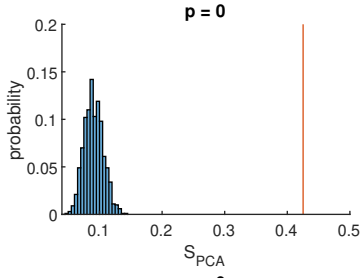
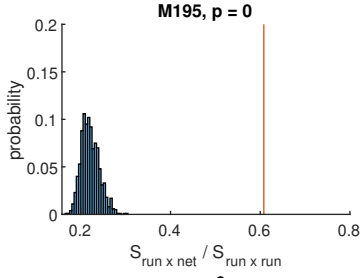
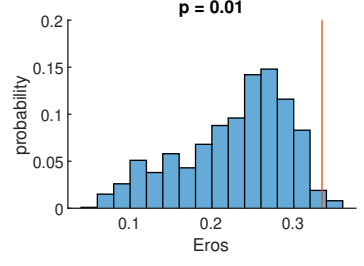
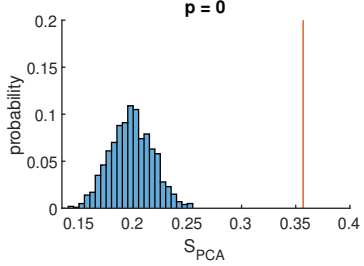
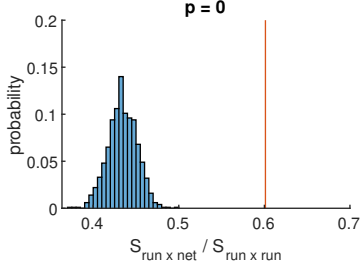
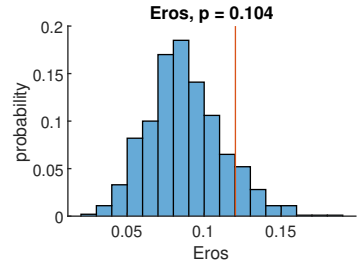
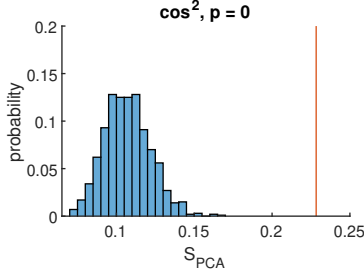
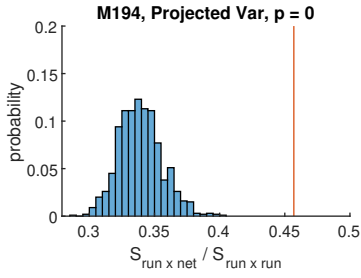


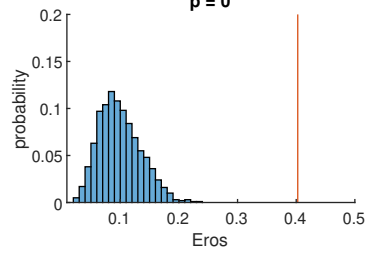
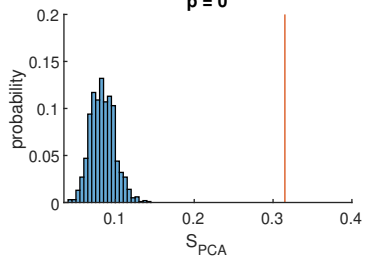
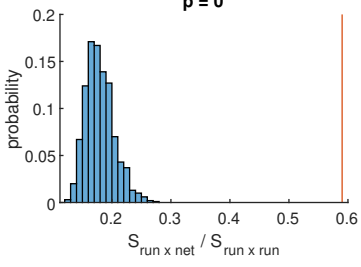
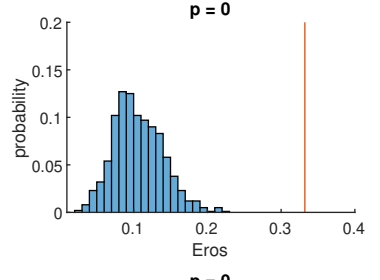
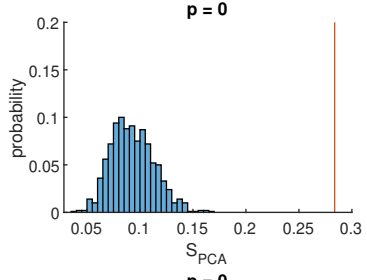
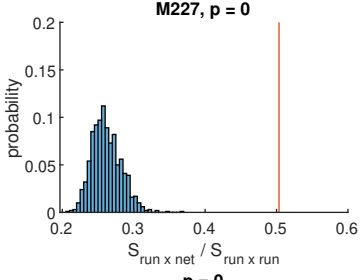
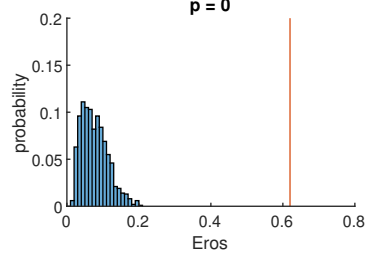
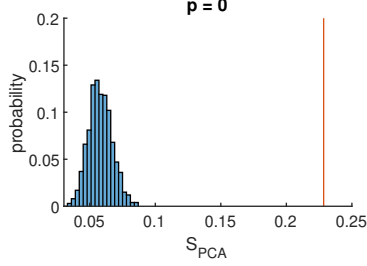
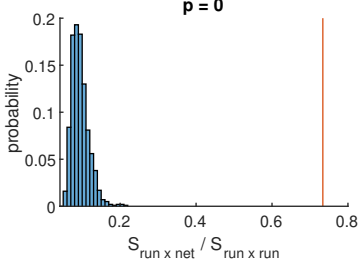
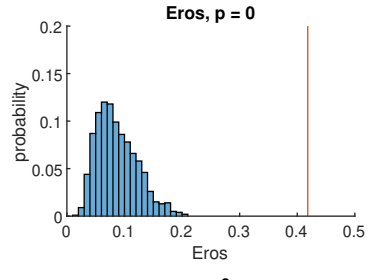
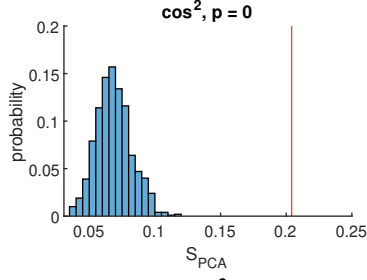
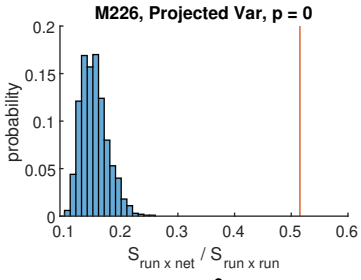


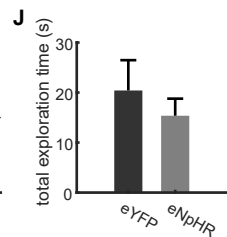
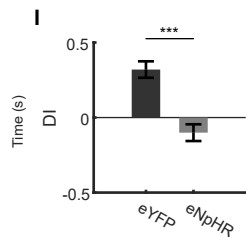
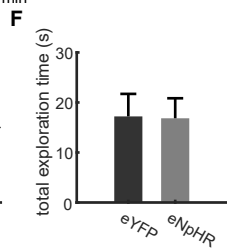
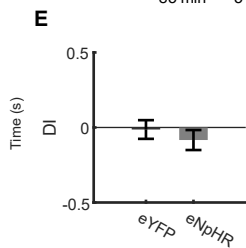
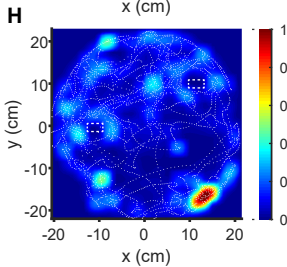
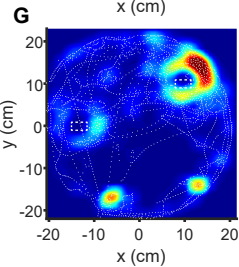
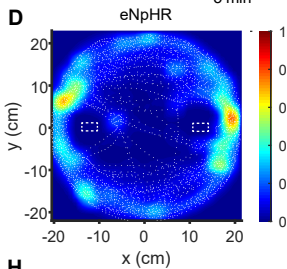
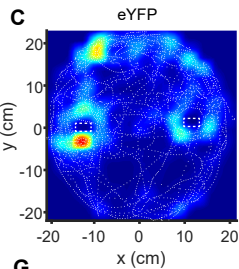
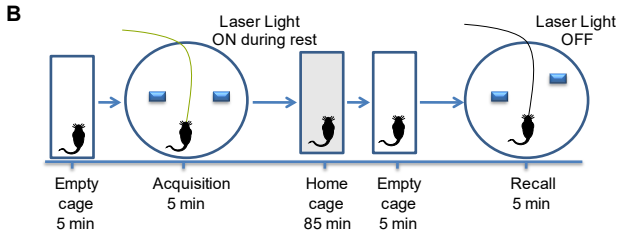
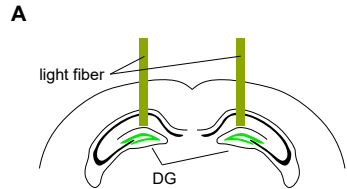
A PCA on DG**B** ICA on DG**C** GPFA on DG**D** PCA on CA1**E** ICA on CA1**F** GPFA on CA1

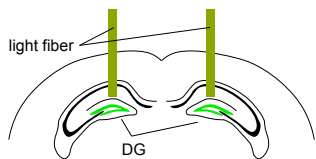
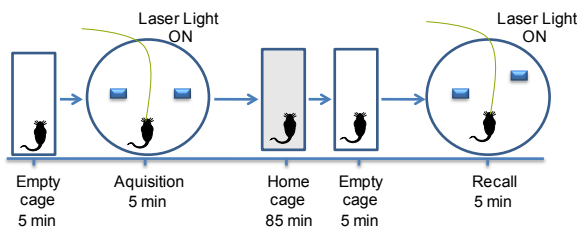
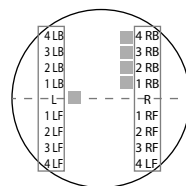
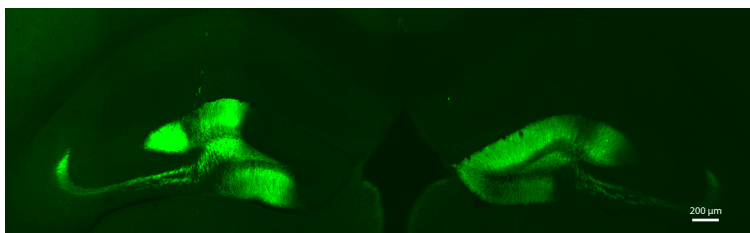
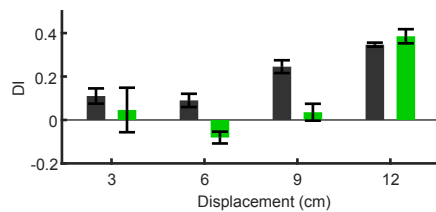
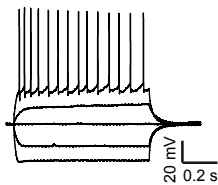
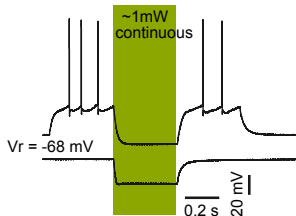
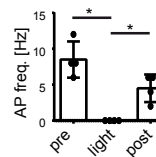
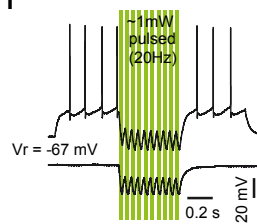
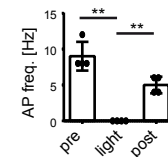
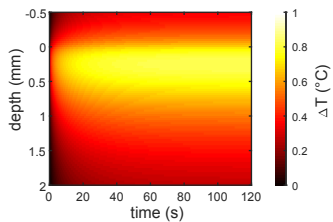
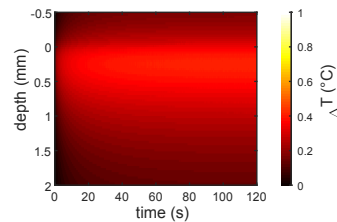










A**B****C****D****E****F****G****H****I****J****K****L****M**